Naval Research Laboratory

Washington, DC 20375-5320

NRL/MR/4790—92-6996

Numerical Modelling of Intense Electron Beam Transport in the Spiral Line Induction Accelerator

J. KRALL, S. SLINKER, M. LAMPE AND G. JOYCE

Beam Physics Branch
Plasma Physics Division

August 28, 1992

REPORT DOCUMENTATION PAGE

Form Approved
OMB No 0704-0188

1. AGENCY USE ONLY (Leave blank)	2. REPORT DATE	3. REPORT TYPE AND DATES COVERED
	August 28, 1992	Interim

4. TITLE AND SUBTITLE

Numerical Modelling of Intense Electron Beam Transport in the Spiral Line Induction Accelerator

5. FUNDING NUMBERS

ARPA Order #7781

6. AUTHOR(S)

J. Krall, S. Slinker, M. Lampe and G. Joyce

7. PERFORMING ORGANIZATION NAME(S) AND ADDRESS(ES)

Naval Research Laboratory
Washington, DC 20375-5320

8. PERFORMING ORGANIZATION REPORT NUMBER

NRL/MR/4790—92-6996

9. SPONSORING/MONITORING AGENCY NAME(S) AND ADDRESS(ES)

DARPA
Arlington, VA 22203

NSWC
Silver Spring, MD 20903-5000

10. SPONSORING/MONITORING AGENCY REPORT NUMBER

11. SUPPLEMENTARY NOTES

12a. DISTRIBUTION/AVAILABILITY STATEMENT

Approved for public release; distribution unlimited.

12b. DISTRIBUTION CODE

13. ABSTRACT *(Maximum 200 words)*

Computer simulation is used to study issues of intense electron beam transport arising in the context of the spiral line induction accelerator (SLIA), a device in which the beam is transported along an open-ended beam pipe, making multiple passes through each accelerating cavity and traversing a 180° achromatic bend between passes. In the straight sections, the beam is transported on a solenoidal field; in the bends, the beam is subject to a vertical bending field and strong focusing stellarator fields, in addition to the solenoidal field. We show that the self-fields of the beam change the optimum vertical field in the bend but do not significantly affect the achromaticity of the bend. We find that magnetic matching elements are required, at the entrance and exit of each stellarator section, to minimize oscillations of the beam envelope and concomitant emittance growth. We show that matching can be accomplished satisfactorily with a single thick quadrupole lens. We determine the frequency and damping rate of envelope oscillations that result from mismatches, and resulting emittance growth. These are found to be sensitive functions of the beam radial profile. Simulation results are found to be in excellent agreement with experiments conducted recently at Pulse Sciences, Inc.

14. SUBJECT TERMS		15. NUMBER OF PAGES
Intense beam	Induction accelerator	63
Emittance growth		16. PRICE CODE

17. SECURITY CLASSIFICATION OF REPORT	18. SECURITY CLASSIFICATION OF THIS PAGE	19. SECURITY CLASSIFICATION OF ABSTRACT	20. LIMITATION OF ABSTRACT
UNCLASSIFIED	UNCLASSIFIED	UNCLASSIFIED	UL

CONTENTS

NUMERICAL MODELLING OF INTENSE ELECTRON BEAM TRANSPORT IN THE SPIRAL LINE INDUCTION ACCELERATOR

I. INTRODUCTION

Advanced high-current accelerator concepts, such as the heavy ion accelerators that are being considered as inertial fusion drivers [1], or the compact high-current electron accelerators [2] that are under development for military and commercial applications, present unique and challenging beam transport problems. In both cases, the beam currents are in the multi-kiloamp regime, where space charge and self-magnetic forces play a major role. In the heavy ion fusion accelerator, both the longitudinal and transverse emittance are strongly constrained by the requirement that the ion beam subsequently be focused, over a focal length of several meters (the radius of the reaction chamber), onto a target with a radius of order 0.2 cm. In the case of high-current electron accelerators, there is considerable interest in generating beams of energetic electrons in very compact devices. To minimize size, multiple-pass designs such as the ion-focused regime recirculator[3], the modified betatron accelerator (MBA)[4] and the spiral line induction accelerator (SLIA)[5] have been investigated. Each of these includes tightly curved transport sections with radii of curvature of order 1 meter. This paper is concerned specifically with the magnetic transport issues that arise in the context of SLIA.

In the proposed design for SLIA (see Fig. 1), the beam is transported along an open-ended beam pipe which makes multiple passes through each accelerating cavity. The accelerating cavities are aligned along the straight sections of the beam pipe, where the beam is transported on a solenoidal focusing field. To bring the beam back around after each straight section, it is taken through a 180° achromatic bend, where a strong focusing stellarator (helical quadrupole) field is provided, in

Manuscript approved June 25, 1992.

addition to the solenoidal field and the vertical bending field. Because the field coils are wound directly onto the spiral beam pipe, and because each bend is magnetically shielded from its neighbors, each bend can be individually designed to be achromatic near the expected beam energy at that point. (A perfectly achromatic bend would be defined as one in which each beam particle exits the bend along the trajectory, relative to the axis, with which it entered the bend.) A schematic diagram of the proposed SLIA proof-of-concept experiment (POCE)[5], which uses three bends and makes two passes though each set of accelerating cores, is shown in Fig. 1.

Two key problems must be addressed in this transport scheme. The first concerns the effect of the hoop forces which act on the beam in the bends. These are the net electrostatic and magnetostatic forces acting on a given beam segment, due to the remainder of the curved beam. Hoop forces have been analyzed only for a coasting beam in a circular torus, such as the MBA.[6] The second difficulty arises from the fact that a matched beam in a solenoid has a circular cross-section, while a matched beam in the combined solenoid/stellarator fields has an elliptical cross-section.[7] Thus it is necessary to use matching elements at the entrance and at the exit of each bend, in order to avoid mismatch oscillations of the beam cross-section which can result in emittance growth. In an higher energy SLIA design, there can be on the order of 10 passes through the accelerating cores[2], implying 19 bends and 38 such transitions.

In this study, we focus our attention on two specific parameter regimes of immediate interest: (1) the POCE, in which a 10 kA, 35 ns beam is to be injected at 3.5 MeV and then accelerated to 9.5 MeV in steps of 1.5 MeV, and (2) recent experiments[8-10] in which an 850 keV, 200 A

injector was used to study the capture of the beam onto a solenoid, and the matching at the entrance of the stellarator field.

These studies are based on numerical simulation. Initially, the simulations were performed using the ELBA three-dimensional particle simulation code[11], which solves Maxwell's equations self-consistently with the complete relativistic beam dynamics. In the ELBA code, the beam pipe is represented as a straight metallic cylinder, but bends are included via a mapping scheme which was adapted from the work of Friedman[12], with corrections to the electromagnetic fields which are valid to first order in the small parameter r_w/R. Here, r_w is the beam pipe radius (3 cm in the POCE) and R is the major radius of the bend (80 cm in the POCE). The electromagnetic field corrections are discussed in the Appendix. The bulk of the studies reported in this paper were done with a faster running version of the code called SST (Single Slice Transport).[13] Here, self-field effects due to variations in the beam density or current along the length of the beam are neglected, so that only a single transverse slice of the beam need be simulated. For transport in a bend, results from the two codes for beam displacement and optimum vertical field showed agreement to within less than 1% for POCE parameters.

The organization of the paper is as follows. In Section II, we discuss the initial equilibrium of the intense beam in the solenoid field. In section III, we present transport simulations for each of the three POCE bends. The optimum vertical field is determined for each bend and compared to the theoretical estimate of Chernin and Sprangle.[6] The effect of this correction to the vertical field on the achromatic properties of the first bend is also assessed. In section IV, we present simulations of transport into and out of the stellarator fields with various beam profiles for POCE

parameters. We show that emittance growth results from phase-mix damping of mismatch oscillations of the beam[14-16], but can be reduced or eliminated though the use of magnetic focusing elements. We present a novel method of accomplishing this match via a single thick quadrupole lens. We present end-to-end simulations of the POCE with and without matching elements. In section V, we discuss the recent experimental results of Refs. 8-10. Simulations with these parameters illustrate the sensitivity of the mismatch oscillation characteristics to the radial distribution of the beam. Our conclusions are given in section VI.

II. EQUILIBRIA FOR SOLENOIDAL TRANSPORT

In accelerator transport studies, it is frequently assumed that the beam has a Kapchinskij-Vladimirskij (K-V) distribution[17] in the rotating frame in the directions (x,y) transverse to the propagation direction (z). The K-V distribution, which has a flat radial density profile, is an exact equilibrium in the limit $\gamma_b \to \infty$ and $\nu/\gamma_b \to 0$, where γ_b is the relativistic factor corresponding to the beam kinetic energy, $\nu = I_b[kA]/17\beta_b$ is Budker's parameter, I_b is the beam current and $\beta_b = (1 - 1/\gamma_b^2)^{1/2}$. However, particle simulations of the POCE beam in the 5.492 kG solenoidal guide field show an instability if the beam is injected with a transverse K-V distribution. The beam radius exhibits growing oscillations at the envelope frequency which typically reach amplitudes of the order of 7 to 10% of the equilibrium radius. These are shown in Fig. 2 (solid line), where the RMS radius r_b is plotted versus transport distance z for the POCE beam (10 kA, 4 MeV, normalized RMS emittance $\varepsilon_{n,rms} = 0.158$ cm-rad) initialized with a K-V distribution. Note that in this simulation and throughout the paper we assume that the diode is nonimmersed, so the canonical angular momentum of the beam is zero. Eventually (over a scale length of several meters), the oscillation amplitude saturates. The instability is a kinetic effect which does not occur in envelope code calculations and is not suppressed by simply initiating the beam with carefully matched envelope parameters. It indicates that the initial distribution is not a true equilibrium, and that the beam dynamics are acting to rearrange the distribution to approach equilibrium. Similar phenomena are seen if the beam is initialized in other distributions that are not exact equilibria for finite ν/γ_b, e.g., a parabolic density profile with a Gaussian velocity distribution. Although the instability is rather

weak, it tends to mask the features of interest. Oscillations of this type are probably inevitable in a real beam, where one does not have perfect control over the beam distribution.

The K-V distribution can be derived from the Vlasov equilibrium given by $f(r,\underline{p}) = n_0/2\pi\gamma_0 m \ \delta(H-\omega L-\gamma_0 mc^2) \ \delta(P-\beta_0\gamma_0 mc)$ in the limit $\gamma_0 \to \infty$.[18] Here the energy H, the canonical angular momentum L, and the canonical axial momentum P are constants of motion and ω, γ_0, β_0 and n_0 are parameters. We have derived an improved distribution by retaining the first order terms in $1/\gamma_0$, which result in corrections to the K-V including the self-generated diamagnetic axial magnetic field and the kinetic energy variations due to the space charge depression.[19] Although the charge distribution is not radially flat in this approximation, it has a sharp cutoff as does the K-V. When the POCE beam is initialized with this higher-order K-V distribution, as in Fig. 2 (dashed line), growing oscillations of the beam radius are not observed.

Simulations of the POCE injector[20], as well as experimental measurements[8-10], indicate that the beam injected into the SLIA transport system has a rounded radial profile, and thus does not have a K-V type distribution. In simulation studies, we have found it convenient to use a numerical technique to initiate the beam equilibrium, rather than the analytic expansion described in the previous paragraph. We begin the simulation with a beam distribution that reflects the macroscopic properties of interest (radial density profile and emittance), and with carefully matched envelope parameters, including an ad hoc correction to the initial particle energy as a function of radius due to the space charge potential of the beam:

$$\gamma = \gamma_b + \frac{\nu}{2}(r^2 - r_b^2)/r_b^2 \ , \qquad (1)$$

where γ is the relativistic factor assigned to a particle at radius r and r_b is the RMS radius of the beam. We have followed this procedure for a variety of equilibria and find that the space-charge correction reduces but does not eliminate the unstable oscillations. The beam is then transported numerically for several meters in the solenoid field, thus allowing the oscillations to saturate and damp. Such equilibria were used to initiate the simulations presented below.

III. TRANSPORT THROUGH THE 180° BEND

Hoop forces occur in the bends because a given point in the curved beam experiences a net transverse electro- and magnetostatic force due to the remainder of the curved beam. These self-fields have been analyzed in some detail for a beam of circular cross-section in a toroidal configuration.[6] Assuming the beam is on axis, the optimum vertical field is given by

$$B_v = \frac{m\gamma_b\beta_b c^2}{eR} + \frac{1}{\beta_b}\frac{mc^2}{e}\frac{\nu}{R}\left[(1+\beta_b^2)\ln\left(\frac{r_w}{r_b}\right) + \delta\beta_b^2\right] \qquad (2)$$

where m is the electron mass, R is the major radius of the bend, r_w is the radius of the beam pipe, e (taken to be positive) is the elementary charge and c is the speed of light. The parameter δ depends on the details of the beam equilibrium in the bend: $\delta = 1$ if one assumes constant current density across the beam cross-section and $\delta = 2$ if one assumes constant circulation frequency. The first term in Eq. (2) is the ideal value for a low-current beam; the second is required to correct for the hoop forces.

For the POCE, in which $I_b = 10$ kA, $R = 80$ cm and $r_w = 3$ cm, these forces can be substantial. In the first bend, for example, the design energy is 4 MeV and the ideal vertical field is 186.9 G. Equation (2) gives B_v between 236.2 G (for δ=1) and 248.6 G (for δ=2). There are additional uncertainties in these values because a) the beam cross-section in the bend is not circular but is instead a slowly rotating ellipse and b) the SLIA bend extends for 180° with entrance and exit points, whereas the published calculation applies to a full toroidal configuration.

Field parameters for the three POCE achromatic bends are given in Table I.[21] In Table I, B_s is the axial magnetic field at the geometric

axis, b_q is the quadrupole field gradient near the quadrupole field axis, and λ_p is the pitch length of the quadrupole windings. The SST and ELBA codes use the following somewhat idealized approximations for the external fields in the bend. The axial field is given by

$$B_z = B_s R/(R + x) \ . \tag{3}$$

The quadrupole fields are

$$B_x = b_q[y \cos(k_q z) - (x - x_q)\sin(k_q z)] \tag{4a}$$

$$B_y = b_q[(x - x_q)\cos(k_q z) + y \sin(k_q z)] \ , \tag{4b}$$

where $k_q = 4\pi/\lambda_p$ and x_q is the x-coordinate of the quadrupole field axis, which is displaced relative to the geometric axis in the bend[22]:

$$x_q = \frac{-r_w^2}{4R}\left[1 + \left(\frac{r_w}{R}\right)^2\right] \ . \tag{5}$$

The vertical field enters as

$$B_y = -B_v(1 - \eta x/R) \tag{6a}$$

$$B_x = B_v \eta y/R \ , \tag{6b}$$

where η is the vertical field index and is responsible for weak focusing in betatrons. In this coordinate system, the beam moves in the z direction, and x and y are the horizontal and vertical coordinates, respectively. The curve lies in the x-z plane with the inside wall of the curved beam pipe at $x = -r_w$. In Eqs. (3-6), we assume $r_w/R \ll 1$.

Each bend is designed to be achromatic near the expected beam energy for that bend. In other words, if the beam is within 10-20% of the design energy for a given bend, the beam should exit with the same position and angle, relative to the axis, that it had when it entered. A perfectly achromatic bend will have no effect on the beam trajectory relative to the axis no matter what the beam energy. In practice, parameters have been determined that are correct to first order in the small parameter $\Delta E/E$ where E is the design energy for the bend and ΔE is the deviation of the beam energy from the design energy.[21,23]

Simulation results for the first bend show that if B_v is set to the value $B_v = 186.9$ G which includes no hoop force corrections, the beam centroid displacement within the bend will exceed 1 cm. This is shown in Fig. 3 where the x and y positions of the beam centroid are plotted versus transport distance for the first POCE bend. Here the bend entrance is located at $z = 50$ cm with the exit at $z = 301.3$ cm. Even with this unacceptably large displacement, the achromatic design brings the centroid back to within 2 mm of the axis on exit. A series of runs were performed to determine the maximum beam centroid displacement $r_{c,max}$ as a function of the imposed B_v. The results are shown in Fig. 4. The optimal value of the vertical field is seen to be 233 G, for which the beam centroid remains within 0.06 cm of the geometric axis at all times. This value of B_v is a 25% increase over the ideal value but is somewhat smaller than expected from Eq. (2). Numerically determined optimum vertical field values for all three bends are given in Table II. For comparison, the ideal values (no hoop force correction) and the predicted values from Eq. (2) are also given.

With a 25% increase in the design value of the vertical field, it might be expected that other corrections to the design parameters of the stellarator and solenoidal fields would be necessary to preserve the achromatic property of the bend. For instance, an achromatic design requires that the frequencies associated with the various fields produce integer numbers of oscillations as the beam traverses the bend. However, Mondelli et al.[24] have shown that the vertical field correction, with an appropriate correction to the vertical field index, simply preserves the frequency that would be expected in the ideal, low-current case. Figures 5 and 6 confirm this conclusion. These figures show the centroid position $x_c(z)$, $y_c(z)$ as the beam passes around the first POCE bend with the optimum vertical field value given in Table I. In Fig. 5, the beam energy was offset from the design energy by $\Delta E = -10\%$. In Fig. 6, $\Delta E = +10\%$. In both cases, the beam centroid returns to within 0.2 cm of the axis.

In principle, it is also necessary to correct the vertical field index η to account for diamagnetic effects in the intense beam, which tend to reduce η to less than the design value over most of the beam cross-section. We have performed several simulations with η set between 0 and 1.0 (at low current, the design value is $\eta = 0.5$). These simulations showed that the value of the vertical field index had less than a 1% effect on the beam centroid position, and had no effect whatsoever on transport at the design energy or the achromatic properties of the first bend. This result might well have been anticipated inasmuch as the strong focusing due to the stellarator fields dominates the weak focusing arising from the betatron field. In subsequent simulations, we simply set $\eta = 0.5$.

We also measured the sensitivity of the achromatic design to errors in the settings of the axial and stellarator magnetic fields. In Figs. 7 and

8, we show the results of setting $\Delta E = -10\%$, and varying B_s and b_q. It is apparent that the achromatic design is tolerant to errors in the 2-3% range and that the design values are not optimized for $\Delta E = -10\%$. Further runs at $\Delta E = +10\%$ showed similar sensitivity to field errors. The optimum values at $\Delta E = +10\%$ differ from those at $\Delta E = 0$ or $\Delta E = -10\%$ but not in an easily predictable way (i.e., corrections to the optimum fields at $\Delta E = +10\%$ are not simply the negatives of those at $\Delta E = -10\%$). These observations are not surprising in that the achromatic parameters are correct only to first order in $\Delta E/E$.

IV. MATCHING VIA MAGNETIC FOCUSING ELEMENTS

A major concern in the SLIA design is the transition at the entrance and exit of each bend. In the straight sections, the beam is transported on a solenoidal field in an equilibrium state with a circular cross-section. In the bends, a strong focusing stellarator (rotating quadrupole) field is also imposed, to improve momentum compaction. Chernin[25] has derived an envelope equation for transport in stellarator/solenoidal fields and has shown that matched solutions exist in which the beam cross-section is elliptic, with constant major and minor radii and with the orientation of the beam ellipse rotating in phase with the stellarator windings. Since the transitions onto and off of the bends will be made more than fifty times in a 50 to 100 MeV accelerator, it is crucial that each transition be made smoothly and with a minimum of emittance growth.

For beams with coupled x-y motion, Chernin[25] has provided a suitable definition of emittance which is a straight-forward generalization of the usual emittance definition (e.g., Ref. 26). This definition is

$$\varepsilon_{rms} \equiv |\Sigma|^{1/4} \tag{7}$$

where Σ is a 4 by 4 matrix with elements

$$\Sigma_{ij} = \langle u_i u_j \rangle - \langle u_i \rangle \langle u_j \rangle \ , \tag{8}$$

$u_1 \equiv x$, $u_2 \equiv dx/dz$, $u_3 \equiv y$, $u_4 \equiv dy/dz$ and "$\langle\ \rangle$" signifies an average over the beam particles. The emittance ε_{rms} is conserved by Chernin's envelope equation[25], which makes the usual assumption that all forces acting on the beam are linear in the radial coordinate r. It is therefore assumed that the beam density profile is flat-topped, which is necessary if the

space-charge forces are to be linear. The normalized, RMS emittance is $\epsilon_{n,rms} = \beta\gamma\epsilon_{rms}$. In terms of the matrix elements Σ_{ij}, the major radius r_+ and the minor radius r_- of the beam cross-section are given by

$$\frac{1}{2}r_{\pm}^2 = \Sigma_{11} + \Sigma_{33} \pm \Sigma_0 \tag{9}$$

where $\Sigma_0 = [(\Sigma_{11} - \Sigma_{33})^2 + 4\Sigma_{13}^2]^{1/2}$. For a beam with circular cross-section, $r_+ = r_- = \sqrt{2}\,r_b$.

Simulations show that large-amplitude envelope oscillations are excited at the entrance and exit of the first POCE bend if no matching lens elements are used to facilitate the transition. The characteristics of the oscillations (wavelength, damping and emittance growth) are not determined entirely by beam envelope parameters but are sensitive to the distribution function of the beam.

In Fig. 9, we show $r_{\pm}(z)$ for the POCE beam as it transits the first bend of the POCE. Four different beam profiles are simulated. In Fig. 9(a), the beam is initiated with a K-V distribution. At the entrance to the bend ($z = 50$ cm), the beam transitions to an elliptic cross-section, but overshoots the elliptic equilibrium and enters into a series of undamped large-amplitude oscillations, which are particularly evident in $r_+(z)$. At the exit from the bend ($z = 301.3$ cm), the beam transitions to an elliptic cross-section of lower eccentricity. After a series of damped oscillations of $r_{\pm}(z)$, the beam approaches an elliptic equilibrium in the solenoidal transport system, but shows no sign of damping back toward the conventional equilibrium with circular cross-section. Little or no emittance increase occurs, as seen in Fig. 10.

This type of behavior is characteristic of the K-V distribution. Because the radial profiles of charge and current density are nearly flat,

the self-forces are nearly linear, there is very little phase-mix damping, and Chernin's envelope equations[25] provide a nearly complete description of the beam dynamics. The damping of the weak oscillations about an elliptic equilibrium in the solenoid is probably associated with self-force nonlinearities that result from the inexactness of the K-V equilibrium, as discussed in Sec. II.

The results are markedly different if the beam profile is rounded, as can be seen in Figs. 9(b)-9(d). In case 9(b), the beam is initiated with a spatially parabolic profile,

$$n_b(r) = \begin{cases} n_b(r=0)[1 - (r/2r_b)^2] , & r \leq 2r_b \\ 0 , & r > 2r_b , \end{cases} \tag{10}$$

where r_b is the RMS beam radius. In Fig. 9(c), the beam is initiated with a Gaussian spatial profile and, in Fig 9(d), with a truncated Bennett[27] spatial profile,

$$n_b(r) = \begin{cases} n_b(r=0)[1 + (r/r_b^2)]^{-2} , & r \leq 3r_b/\sqrt{2} \\ 0 , & r > 3r_b/\sqrt{2} . \end{cases} \tag{11}$$

Each of our non-K-V beams have Gaussian distribution functions in velocity space. In each of these cases, the beam becomes mismatched at the stellarator entrance, damps toward an elliptical state in the bend, becomes mismatched again at the exit, and finally damps toward a circular cross-section. Each stage of damping is accompanied by emittance growth as seen in Fig. 10. The damping would appear to be associated with phase mixing,

due to the nonlinear self-field forces arising from the rounded beam radial profiles. Since rounded beam profiles are typical in the SLIA, the pictures presented in Figs. 9(b-d) are representative of SLIA physics, rather than the K-V case, Fig 9(a), where the oscillations are highly coherent and undamped. We can expect considerable emittance growth in the accelerator unless lens elements are introduced to carefully match the beam at the entrance and exit of each bend.

Tiefenback[9] has shown that the beam envelope parameters Σ_{ij} can be matched exactly by using a compound magnetic lens consisting of three ideal thin focusing elements (one solenoid lens and two quadrupole lenses). Petillo et al.[21] have used an envelope code to show that this scheme can be implemented with realistic, finite thickness lenses to obtain a useful inexact match. We have found a novel solution to the matching problem which employs a single thick quadrupole lens.

The key to this matching scheme is the effect of a thick quadrupole lens on beam transport in a solenoidal field. This is illustrated in Fig. 11, where we plot the major and minor radii $r_{\pm}(z)$ obtained from solutions of the envelope equations with beam and solenoidal field parameters corresponding to those of the first POCE bend. A thin quadrupole lens, Fig. 11(a), simply induces a series of quasiperiodic quadrupole envelope oscillations, i.e., the beam cross-section oscillates between states of maximum elliptic eccentricity, passing through a circular cross-section in between maxima. However, when the quadrupole lens has finite thickness L_Q [defined as the full-width-at-half-maximum length of the field envelope $b_Q(z)$], as in Fig. 11(b), the traces of $r_+(z)$ and $r_-(z)$ separate, so that the cross-section is non-circular at all times, but oscillates between states of maximum and minimum elliptic eccentricity. As the thickness of

the lens increases further, to L_Q = 5 cm in Fig. 11(c), $r_+(z)$ and $r_-(z)$ become well separated, and oscillate separately around central values corresponding to an elliptic equilibrium state. For a still thicker lens, L_Q = 10 cm in Fig. 11(d), $r_+(z)$ performs small-amplitude sinusoidal oscillations about a well-defined equilibrium value and phase locking is observed such that $r_-(z)$ is approximately stationary at the extrema of $r_+(z)$. The beam has been transformed from its initial circular equilibrium to a new approximate equilibrium in which the cross-section is elliptic and slowly rotating. The eccentricity of the ellipse is nearly constant and is determined by the integrated strength of the lens $\int dz\, b_Q(z)$. Recall, however, that in the context of a more exact kinetic treatment, rather than an envelope model, the elliptic equilibrium will eventually damp back to circular if there is phase mixing due to a rounded beam radial profile (see Fig. 9). The transition to an elliptic equilibrium via a single quadrupole lens and subsequent damping toward a circular beam cross-section has been observed both experimentally[22] and in particle simulations.

Envelope modelling and particle simulations indicate that the beam response to a quadrupole lens is not very sensitive to the details of the quadrupole lens axial dependence $b_Q(z)$, but rather depends primarily on the integrated lens strength $\int dz\, b_Q(z)$ and on the thickness L_Q. An approximate criterion for the "thick lens" limit, as exemplified by Fig. 11(c) and to an even greater degree by Fig. 11(d), is

$$L_Q > \frac{\lambda_c}{4} = \frac{\pi\gamma mc^2}{2eB_s} , \qquad (12)$$

where λ_c is the cyclotron wavelength in the solenoidal field. (For SLIA parameters, the oscillation wavelength is not significantly increased by

space-charge fields.) In the first POCE bend, λ_c = 17.2 cm, and the lens is "thick" in Figs. 11(c) and 11(d), where L_Q = 5 cm and 10 cm, respectively.

The matching onto the stellarator equilibrium is accomplished by using a quadrupole lens that is in the "thick lens" limit (given the beam energy at that point in the beam line), adjusting the integrated strength of the lens to match the eccentricity needed in the bend, adjusting the distance between the lens and the bend such that the beam enters the stellarator field at a stationary point of the oscillation, and adjusting the orientation of the lens so that the angle of the ellipse is in the correct phase as the beam enters the bend. A single quadrupole lens can also be used at the exit of the bend to bring the beam back to a nearly circular cross-section. In the ideal case (no envelope oscillations), the exit quadrupole is identical to the entrance quadrupole.

It should be noted that the required minimum lens thickness L_Q, such that the lens is "thick," increases proportionally to the beam energy, according to Eq. (12). For example, the lens of Fig. 11(c) is sufficiently thick for the first bend of the POCE (electron energy 4 MeV), but not for the third bend (7 MeV), as shown in Fig. 12. For practical reasons, it may be necessary to use another matching scheme at high energy.

Although the features of the matching scheme are easily accessed and surveyed by numerically solving the envelope equations, we have used particle simulation to study the transport processes in full detail. Figures 13 and 14 show the results of a simulation of transport around the POCE first bend for a case in which the beam is initiated with a parabolic radial profile identical to that of Fig. 9 (b). Here, a single quadrupole lens is used to match the beam at the entrance to the bend. The lens is

located 25 cm from the stellarator entrance, with peak quadrupole gradient b_Q = 292 G/cm, z-dependence as plotted in Fig. 15 and lens thickness L_Q = 5.5 cm. At the bend exit, we fine-tuned the match using an exit quadrupole with b_Q = 255 G/cm (this fine tuning accounts for the phase of the small mismatch oscillation as the beam exits the stellarator). The lens profile of Fig. 15 is taken from measurements of an actual quadrupole lens used in SLIA experiments.[22] With this matching scheme, the radial mismatch oscillations of Fig. 9(b) have been minimized and the 13% emittance growth of the unmatched case has been eliminated. For comparison, Fig. 14 shows emittance plotted versus transport distance for this case and for the simulation of Fig. 9(b). We have obtained similar results via the three-element match of Ref. 21.

These simulations have been extended to provide complete end-to-end particle simulations of transport in the POCE with each of the three bends modeled as described above. The acceleration sections are modeled by simply imposing an axial electric field over a short section of the beam pipe. The location of each curve and each idealized acceleration section for the end-to-end simulations is given in Table III. Results from a simulation without matching elements are shown in Fig. 16. The beam is initiated with a parabolic spatial profile as in Figs. 9(b) and 13 above. Overall, the emittance $\varepsilon_{n,rms}$ increases by 52%. Plots of $r_{\pm}(z)$ show that the beam becomes mismatched in each bend and damps back to an approximately circular cross-section after each bend. It is interesting to note that, by chance, the beam exits the third bend with an approximately circular cross-section and little subsequent emittance growth occurs. For comparison, we repeated this simulation with the third bend terminated at z = 1250 cm, at

the point of maximum eccentricity of the beam cross-section. In this case we observed an overall emittance increase of 110%.

The results of an end-to-end POCE simulation in which single-element matching is employed on all three bends are shown in Fig. 17. Here, the initial beam parameters are identical to those of Fig. 16. With the use of single-element matching, however, the normalized emittance is largely preserved, increasing by only 10%. In this simulation, quadrupole lenses with peak quadrupole gradient b_Q = 149 G/cm were placed 4 cm from the entrance and 4 cm after the exit of the second bend. For the third bend, lenses were located 6 cm from the stellarator end points with b_Q = 266 G/cm. The quadrupole lens profile of Fig. 15 was used for the first bend, as in Fig. 13, and a similarly shaped quadrupole with L_Q = 11 cm was used on the second and third bends.

V. SIMULATION OF THE 850 KeV EXPERIMENT

In preparation for the POCE, a series of preliminary transport and matching experiments has recently been performed at PSI.[8-10] The parameters for these experiments were chosen to replicate as closely as possible the physics of the POCE beam at much lower current and energy. Thus, the dimensionless ratio $\sigma = \nu r_b^2/\gamma\varepsilon_n^2$, which determines the relative influences of the emittance and space charge forces, was chosen to be the same for both beams. The significance of σ can be noted from the envelope equation for a beam in the presence of an axial magnetic field[28,15],

$$\frac{\partial^2 r_b}{\partial z^2} + \frac{\Omega_z^2}{4\beta_b^2 c^2 \gamma_b^2} r_b - \frac{2\nu}{\beta_b^2 \gamma^3 r_b} - \frac{\varepsilon_n^2}{\beta_b^2 \gamma_b^2 r_b^3} = 0 , \qquad (13)$$

where $\Omega_z = eB_z/mc$ is the nonrelativistic cyclotron frequency and $\varepsilon_n = 4\varepsilon_{n,rms}$. The nominal POCE parameters are $I_b = 10$ kA, $\gamma_b = 8.83$ (4 MeV), $\varepsilon_{n,rms} = 0.159$ cm-rad and $r_b = 0.5$ cm, which gives $\sigma = 0.041$. The low energy experiments were done at $I_b = 200$ A, $\gamma_b = 2.66$ (850 keV), and $r_b = 0.25$ cm. Preservation of the ratio σ requires $\varepsilon_{n,rms} = 0.022$ cm-rad (the actual experimental value was somewhat lower, as will be discussed below). In these experiments, the beam was transported along a 1.5 kG solenoid field into a stellarator section with length 251.3 cm and pitch $\lambda_p = 68.33$ cm, identical to that of the first POCE bend. This stellarator section, however, was straight (rather than curved) so as to facilitate diagnostics, and the stellarator strength was reduced to $b_q = 68.5$ from the POCE value of 251.6 G/cm.

In the initial experiment, the beam was transported into the stellarator fields without matching at the stellarator entrance. The data from this experiment, giving the beam major and minor radii $r_\pm(z)$, are

shown in Fig. 18. Each data point represents a time-integrated average over one shot of the device, obtained by inserting a piece of film into the beam pipe at a location that was varied from shot to shot. It should be noted that the experimental "major and minor radii" $r_{\pm}(z)$ are determined by fitting a constant current-density contour at approximately 10% of the peak current density in each shot, whereas the simulation $r_{\pm}(z)$ values are computed via Eq. (9) and are RMS values multiplied by $\sqrt{2}$. The experimental measurements extend only to $z = 350$ cm, 50 cm beyond the end of the stellarator section. As a result, the damping of mismatch oscillations at the stellarator exit, as well as the emittance growth associated with this damping, was not measured. The simulations extend to $z = 500$ cm, enabling us to study matching phenomena at the exit as well as the entrance of the stellarator section.

In Fig. 18, it is evident that envelope oscillations are excited at the stellarator entrance which subsequently damp toward an elliptic equilibrium. Emittance measurements, which tend to be problematical for a space-charge dominated beam, were made both at the injector and at the exit of the stellarator section. The inherent difficulties associated with this measurement were further exacerbated at the end of the stellarator section by the need to aperture the beam and to transport the resulting "beamlet" into a field-free region. Because the measurement was performed within the 3 cm radius beam pipe, the drift region over which the emittance could be measured was limited to 10 cm. In fact, a definitive measurement of the emittance at the stellarator exit has not yet been obtained.[22]

Preliminary measurements of the beam initial radial profile showed an approximately parabolic profile with emittance $\varepsilon_{n,rms} = 0.008$ rad-cm and beam radius 0.25 cm.[22] In our first simulation studies, we initiated the

beam with a parabolic profile. One such simulation is shown in Fig. 19, with beam parameters r_b = 0.25 cm, $\varepsilon_{n,rms}$ = 0.011 rad-cm. The damping rate was found to be comparable to that of the experiment, but the mismatch oscillation frequency differs markedly (by 25%) from that seen in the experiment. It was found to be impossible to match the experimental data in simulations initiated with any of the usual distributions (KV, parabolic, Gaussian, Bennett).

Since it is known[29] that core-halo radial profiles are associated with increased phase-mix damping of radial mismatch oscillations expected to be present in the injector[10,20], we then tried initiating the beam with a core-halo profile in the simulations. It was found that the simulations could provide a good match to the data. Subsequently, careful measurements were performed which indicated that the beam had approximately 10% of its current in a diffuse halo extending to about twice the radius of the main core, as shown in Fig. 20.

Creating a core-halo distribution for simulation purposes was accomplished by adding a constant density spatial distribution with edge radius $2r_b$ to the core parabolic distribution. The result was then transported for 30 meters and allowed to come to equilibrium. The spatial profile of our numerical core-halo distribution is shown in Fig. 21. Here, we put 25% of the current into the initial flat-top halo. In the resulting beam, particles with $r > r_+ = 3.46$ mm represented 8% of the total current. In Fig. 21, the beam emittance is $\varepsilon_{n,rms}$ = 0.01 cm-rad. If we consider only the particles within the $r \leq r_+$ we have $\varepsilon_{n,rms}$ = 0.0065 cm-rad.

Figure 22 shows the major and minor radii $r_\pm(z)$ and the emittance $\varepsilon_{n,rms}(z)$ of the core-halo simulation beam. The simulation reproduces the

radial oscillation frequency and the damping rate observed in the experiments. Total emittance growth in the simulation was 29%.

Experiments were also done using the three-element match of Ref. 21. Experimental major and minor radii, again defined in terms of the time-averaged current-density contour at 10% of the peak current density, are plotted versus transport distance in Fig. 23. In this case, the mismatch oscillations are greatly reduced.

Simulation results using the core-halo distribution as in Fig. 22 are shown in Fig. 24. Here we have used a single-element match with peak quadrupole gradient b_Q = 75 G/cm located 5 cm from the stellarator entrance. As before, the axial lens profile is that shown in Fig. 15. We find smaller radial oscillations, as in the experiment, and emittance growth of only 11%.

VI. CONCLUSIONS

Simulation studies of recent SLIA experiments and of the SLIA POCE have been performed. Simulation results showed that as the intense beam is transported through each bend, the beam experiences self electro- and magnetostatic forces. To account for these forces, the design value of the vertical bending field had to be increased by as much as 25%. Optimum vertical field values, which were in reasonable agreement with the theoretical analysis of Ref. 6, were determined for each bend. Furthermore, we found that this correction to the vertical field did not adversely effect the chromatic properties of the bend.

Simulations of transport into the stellarator fields showed that radial mismatch oscillations are likely to be excited both at the stellarator entrance and at the exit. Simulation results were quite sensitive to the spatial distribution of the beam particles. We found that, if the radial profile of the beam is rounded, the mismatch oscillations damp and that this damping is accompanied by emittance growth. These phenomena did not occur when the beam was initialized with a Kapchinskij-Vladimirskij distribution, however. We believe that the observed damping of radial mismatch oscillations is due to phase mixing caused by nonlinear space-charge forces associated with a non-uniform beam profile.[14-16] By contrast, the K-V distribution has a uniform spatial profile.

We have presented a novel method of matching the beam onto and off of the stellarator fields. Here we use a single thick quadrupole lens on each end of the stellarator to transform the circular cross-section of the beam in the solenoid field into an elliptical shape that closely approximates the equilibrium configuration in the stellarator fields. The lens strength

and orientation are adjusted to obtain the correct eccentricity and phase at the stellarator entrance. An identical lens, with only its orientation adjusted, is used at the exit to bring the beam back to a circular cross-section. Simulations show that matching can be accomplished in this way and that the degree of emittance growth can be greatly reduced by the use of such single-element matching lenses.

We also performed end-to-end simulations of the SLIA POCE, where the beam was taken through all three bends. These showed that matching elements can reduce total emittance growth from 52% to 10%. While the level of emittance growth found in the end-to-end simulations was modest even when no matching elements were used, such elements will certainly be necessary in a 50-100 MeV SLIA design, where many more bends would be required.

We have also explored other approaches to the SLIA matching and transport problems, which are not reported here. For instance, discrete, alternating-gradient quadrupole lenses were considered as an alternative to stellarator windings. The motivation for this study was the possibility of improved stability with regard to the electromagnetic instability of Refs. 30-32. It was found, however, that alternating-gradient transport is comparably unstable.[33,34] It was further found that the instability could be avoided in the stellarator configuration by carefully choosing system parameters.[31,32,35] We also considered a design in which stellarator windings were used on the straight sections as well as on the bends. This design does not avoid the complication of changing the parameters of the stellarator and solenoid fields between each bend, in order to keep the bends achromatic as the beam energy increases. We found that the stellarator-stellarator transitions (i.e., between the parameters

of bends one and two) were no less problematical than the solenoid-stellarator transitions of the POCE. This difficulty persisted even for designs in which each bend had the same stellarator pitch length.

Finally, simulations were performed to model and understand the recent SLIA transport experiments.[8-10] A core-halo distribution, similar to that of the 850 keV, 200 A experimental beam, was used in simulations of transport through the stellarator fields, with and without matching lenses. These simulations reproduced each of the key features of the experiments, including the motion of the beam cross-section, which followed the pitch of the stellarator windings in all cases, the amplitude, frequency and damping rate of the radial mismatch oscillations, and the reduction in the amplitude of these oscillations through the use of matching elements at the stellarator entrance and exit.

In the 850 keV simulations, the sensitivity of the results to the spatial distribution of the beam was of key importance in our efforts to reproduce the experimental results. Specifically, the initial measurements of the spatial profile of the beam showed only the central core. Simulation results with the same profile (Fig. 19) showed a 25% disparity in the frequency of the mismatch oscillations between simulation and experiment (see Fig. 18). By adding a halo, we found that this disparity could be eliminated. The addition of a halo was motivated by the fact that such core-halo distributions are associated with the damping of radial mismatch oscillations[29] as might be present in the injector.[10,20] The existence of the halo was later confirmed experimentally.[10]

ACKNOWLEDGMENTS

We wish to acknowledge our collaboration with V. Bailey, M. Tiefenback, J. Lidestri, D. Wake and S. Putnam of Pulse Sciences, Inc., who assisted us in interpreting their experimental data. We also wish to acknowledge many helpful discussions with J. Petillo, D. Chernin and A. Mondelli of Science Applications International Corp., T. Hughes of Mission Research Corp., I. Haber, C. M. Tang and R. Hubbard of N.R.L. and M. Reiser of the University of Maryland.

This work was supported by Defense Advanced Research Projects Agency under ARPA Order 7781 and monitored by the Naval Surface Warfare Center.

APPENDIX: FIRST ORDER FIELD CORRECTIONS IN A CURVED GEOMETRY

In the ELBA[11] and SST[13] particle simulation codes, the electromagnetic fields are computed in terms of the scalar and vector potentials using cylindrical coordinates. In all cases, the beam is assumed to be propagating within a conducting pipe of radius r_w. Following the approach originated by Lee[36], the equations are solved using the gauge

$$\nabla_\perp \cdot \underline{A}_\perp = 0 \ , \tag{A1}$$

where $\underline{A}_\perp$ is the component of the vector potential perpendicular to the direction of propagation. This gauge works well for problems in which the beam is nearly axisymmetric and dominates the field production. In the ELBA code, a change of variables is made from (r,θ,z,t) to $(r,\theta,\zeta=ct-z,\tau=t)$. The (ζ,τ) variables are numerically advantageous in that a) a relativistic beam is nearly stationary in these coordinates and b) information flow is always towards larger values of ζ. The SST code makes the additional simplifying assumption that $\partial/\partial\zeta = 0$. This approximation is useful when self-forces arising from ζ-derivatives of the beam density and current can be neglected.

In terms of the potentials, $\underline{A}_\perp$, Φ and $\alpha \equiv A_z - \Phi$, Maxwell's equations in the gauge of Eq. (A1) can be written as[11,37]

$$\nabla_\perp^2 \Phi + \frac{\partial E_z}{\partial \zeta} = -4\pi\rho \ , \tag{A2}$$

$$\nabla_\perp^2 \alpha + \frac{1}{c}\frac{\partial E_z}{\partial \tau} = -4\pi(J_z/c - \rho) \tag{A3}$$

and

$$\nabla_{\perp}^2 \underline{A}_{\perp} - \frac{1}{c}\frac{\partial}{\partial\tau}\left(\frac{1}{c}\frac{\partial}{\partial\tau} + 2\frac{\partial}{\partial\zeta}\right)\underline{A}_{\perp} = -\frac{4\pi}{c}\underline{J}_{\perp} - \nabla_{\perp}\left(\frac{\partial\alpha}{\partial\zeta} - \frac{1}{c}\frac{\partial\Phi}{\partial\tau}\right) , \qquad (A4)$$

where

$$E_z = -\left(\frac{1}{c}\frac{\partial}{\partial\tau} + \frac{\partial}{\partial\zeta}\right)\alpha - \frac{1}{c}\frac{\partial\Phi}{\partial\tau} . \qquad (A5)$$

For propagation around a bend, we neglect corrections to A_r and A_θ and retain terms in the equations for α and Φ to first order in r_w/R, where R is the radius of curvature of the bend. The corrections are treated as explicit terms in the solution algorithms. Maxwell's equations for the potentials in the bend are derived by transforming to a local orthogonal coordinate system (r,θ,s) which is centered on the axis of the beam pipe with s measuring arc length along the bend. The (r,θ,s) coordinates can be written in terms of global Cartesian coordinates (x,y,z) with the origin at the center of the bend:

$$x = (R + r\cos\theta)\cos(s/R) , \qquad (A6a)$$

$$y = r\sin\theta \qquad (A6b)$$

and

$$z = (R + r\cos\theta)\sin(s/R) , \qquad (A6c)$$

for $r \leq r_w$.

Maxwell's equations for α and Φ are written in the (r,θ,s) coordinate system and expanded to first order in r/R. We then make a change of variables from (r,θ,s,t) to $(r,\theta,\zeta=ct-s,\tau=t)$. The result is

$$\nabla_\perp^2\Phi + \frac{\partial E_s}{\partial\zeta} = -4\pi\rho - \frac{1}{R}\Big[\cos\theta\,\frac{\partial\Phi}{\partial r} - \frac{\sin\theta}{r}\,\frac{\partial\Phi}{\partial\theta} + \frac{r}{c}\cos\theta\,\frac{\partial^2\Phi}{\partial\tau\partial\zeta}$$

$$+ \frac{r}{c}\cos\theta\,\frac{\partial^2\alpha}{\partial\tau\partial\zeta} + r\cos\theta\,\frac{\partial^2\alpha}{\partial\zeta^2} + \cos\theta\Big(\frac{1}{c}\,\frac{\partial A_r}{\partial\tau} + \frac{\partial A_r}{\partial\zeta}\Big)$$

$$- \sin\theta\,\Big(\frac{1}{c}\,\frac{\partial A_\theta}{\partial\tau} + \frac{\partial A_\theta}{\partial\zeta}\Big)\Big] \qquad \text{(A7)}$$

and

$$\nabla_\perp^2\alpha + \frac{1}{c}\,\frac{\partial E_s}{\partial\tau} = -4\pi(J_z/c - \rho)$$

$$+ \frac{1}{R}\Big[r\cos\theta\Big(\frac{1}{c}\,\frac{\partial^2\Phi}{\partial\tau\partial\zeta} + \frac{1}{c}\,\frac{\partial^2\alpha}{\partial\tau\partial\zeta} + \frac{\partial^2\alpha}{\partial\zeta^2}\Big) - \cos\theta\,\frac{\partial\alpha}{\partial r}$$

$$+ \frac{\sin\theta}{r}\,\frac{\partial\alpha}{\partial\theta} + \cos\theta\Big(2\frac{\partial A_r}{\partial\zeta} + \frac{1}{c}\,\frac{\partial A_r}{\partial\tau}\Big)$$

$$- \sin\theta\Big(2\frac{\partial A_\theta}{\partial\zeta} + \frac{1}{c}\,\frac{\partial A_\theta}{\partial\tau}\Big)\Big]\,, \qquad \text{(A8)}$$

where

$$E_s = -\Big(\frac{1}{c}\,\frac{\partial}{\partial\tau} + \frac{\partial}{\partial\zeta}\Big)\alpha - \frac{1}{c}\,\frac{\partial\Phi}{\partial\tau} - \frac{r}{R}\cos\theta\,\frac{\partial\Phi}{\partial\zeta} \qquad \text{(A9)}$$

and J_s is the current density in the s direction. Because we neglect corrections to A_r and A_θ, the gauge condition, Eq. (A1), and Eq. (A4) remain unchanged. The remaining electric and magnetic field components are

$$E_r = -\frac{1}{c}\,\frac{\partial A_r}{\partial\tau} - \frac{\partial A_r}{\partial\zeta} - \frac{\partial\Phi}{\partial r}\,, \qquad \text{(A10a)}$$

$$E_\theta = -\frac{1}{c}\frac{\partial A_\theta}{\partial \tau} - \frac{\partial A_\theta}{\partial \zeta} - \frac{1}{r}\frac{\partial \Phi}{\partial \theta}\ , \qquad \text{(A10b)}$$

$$B_r = \frac{1}{r}\frac{\partial \alpha}{\partial \theta} + \frac{1}{r}\frac{\partial \Phi}{\partial \theta} + \frac{\partial A_\theta}{\partial \zeta} - \frac{1}{R}[r\cos\theta\frac{\partial A_\theta}{\partial \zeta} + \sin\theta(\alpha + \Phi)]\ , \qquad \text{(A11a)}$$

$$B_\theta = -\frac{\partial A_r}{\partial \zeta} - \frac{\partial \alpha}{\partial r} - \frac{\partial \Phi}{\partial r} + \frac{1}{R}[r\cos\theta\frac{\partial A_r}{\partial \zeta} - \cos\theta(\alpha + \Phi)] \qquad \text{(A11b)}$$

and

$$B_s = \frac{1}{r}\frac{\partial}{\partial r}(rA_\theta) - \frac{\partial A_r}{\partial \theta}\ . \qquad \text{(A11c)}$$

References

1. C. G. Fong, T. J. Fessenden, R. L. Fulton and D. Keefe, in Proceedings of the 1989 IEEE Particle Accelerator Conference, IEEE Catalog No. 89CH2669-0 (Chicago, IL, 1989), p. 962.
2. S. D. Putnam, in Proceedings of the 1987 IEEE Particle Accelerator Conference (New York, IEEE Press, 1987) p. 887.
3. W. K. Tucker, S. L. Shope and D. E. Hasti, in Proceedings of the 1987 IEEE Particle Accelerator Conference (New York, IEEE Press, 1987) p. 957.
4. C. A. Kapetanakos, L. K. Len, T. Smith, J. Golden, K. Smith, S. J. Marsh, D. Dialetis, J. Mathew, P. Loschialpo and J. H. Chang, Phys. Rev. Lett. 64, 2374 (1990); C. W. Roberson, A. Mondelli and D. Chernin, Phys. Rev. Lett. 50, 507 (1983).
5. V. Bailey, L. Schlitt, M. Tiefenback, S. Putnam, A. Mondelli, D. Chernin, and J. Petillo, in Proceedings of the 1987 IEEE Particle Accelerator Conference (New York, IEEE Press, 1987), p. 920; A. Mondelli, D. Chernin, S. D. Putnam, L. Schlitt and V. Bailey, in Proceedings of the Sixth Inernational Conference on High Power Particle Beams (Osaka, Japan, 1986).
6. D. Chernin and P. Sprangle, Part. Accel. 12, 85 (1982).
7. R. L. Gluckstern, in Proceedings of the 1979 Linear Accelerator Conference, BNL Report BNL-51134 (Brookhaven, New York, 1979), p. 245.
8. J. P. Lidestri, V. L. Bailey, Jr., J. A. Edighoffer, S. D. Putnam, M.G. Tiefenback and D. Wake, in Conference Record of the 1991 IEEE Particle Accelerator Conference, IEEE Catalog No. 91CH3038-7 (San Francisco, CA, 1991), p. 3120.

9. M. G. Tiefenback, J.P. Lidestri, V.L. Bailey, Jr. and S.D. Putnam, in Conference Record of the 1991 IEEE Particle Accelerator Conference, IEEE Catalog No. 91CH3038-7 (San Francisco, CA, 1991), p. 3195.

10. M. G. Tiefenback, S. D. Putnam, V. L. Bailey, Jr., J. P. Lidestri and J. A. Edighoffer, PSI Report PSIFR-2543-01 (1991).

11. G. Joyce, J. Krall, and S. Slinker, in Proceedings of the Conference on Computer Codes in the Linear Accelerator Community, LANL Report LA-11857-C (Los Alamos, NM, 1990), p. 99; S. Slinker, G. Joyce, J. Krall and R. F. Hubbard in Proceedings of the 14th International Conference on the Numerical Simulation of Plasmas (Annapolis, MD, 1991).

12. A. Friedman, in Proceedings of the 13th International Conference on the Numerical Simulation of Plasmas (Santa Fe, NM, 1989); A. Friedman, D. A. Callahan, D. P. Grote, A. B. Langdon and I. Haber, in Proceedings of the Conference on Computer Codes in the Linear Accelerator Community, LANL Report LA-11857-C (Los Alamos, NM, 1990), p. 119.

13. J. Krall, G. Joyce and S. Slinker, in Proceedings of the 14th International Conference on the Numerical Simulation of Plasmas (Annapolis, MD, 1991).

14. S. Humphries, Charged Particle Beams (J. Wiley, New York, 1990).

15. J. D. Lawson, The Physics of Charged Particle Beams, Second Edition (Oxford U. P., London, 1988).

16. T. P. Wangler, K. R. Crandall, R. S. Mills and M. Reiser, IEEE Trans. Nucl. Sci NS-32, 2196 (1985).

17. I. M. Kapchinskij and V. V. Vladimirskij, in Proceedings of the International Conference on High-Energy Accelerators and Instrumentation (CERN, 1959), p. 274.

18. R. C. Davidson, Physics of Nonneutral Plasmas (Reading, MA, Addison-Wesley, 1990), pp. 588-594.

19. S. Slinker, G. Joyce, J. Krall and M. Lampe, submitted to Phys. Fluids B.

20. T. P. Hughes, T. C. Genoni, K. T. Nguyen and D. R. Welch, MRC Report MRC/ABQ-R-1442 (1991).

21. J. J. Petillo, C. Kostas, D. P. Chernin and A. Mondelli, in Conference Record of the 1991 IEEE Particle Accelerator Conference, IEEE Catalog No. 91CH3038-7 (San Francisco, CA, 1991), p. 613; The parameters listed in Table I of this reference are for the case of zero space-charge and are useful for the envelope code simulations included therein. The parameters for our case were generated in the same way, but with some space-charge effects included.

22. V. Bailey and J. Lidestri, private communication.

23. V. Bailey, D. Wake, R. Curry, J. Lidestri and M. Tiefenback, in Conference Record of the 1991 IEEE Particle Accelerator Conference, IEEE Catalog No. 91CH3038-7 (San Francisco, CA, 1991), p. 3123.

24. A. Mondelli, D. Chernin and J. Petillo, private communication.

25. D. Chernin, Part. Accel. 24, 29 (1988).

26. F. J. Sacherer, IEEE Trans. Nucl. Sci 18, 1105 (1971).

27. W. H. Bennett, Phys. Rev. 45, 890 (1934).

28. E. P. Lee and R. K. Cooper. Part. Accel. 7, 83 (1976).

29. See, e.g., Y.-J. Chen, G. J. Caporaso, A. G. Cole, A. C. Paul and W. C. Turner, in Conference Record of the 1991 IEEE Particle Accelerator Conference, IEEE Catalog No. 91CH3038-7 (San Francisco, CA, 1991), p. 3100 and D. Kehne, M. Reiser and H. Rudd, ibid., p. 248.

30. T. P. Hughes and B. B. Godfrey, Phys. Fluids 29, 1698 (1986).

31. C. M. Tang, P. Sprangle, J. Krall, P. Serafim and F. Mako, Part. Accel. 35, 101 (1991).

32. J. Krall, C. M. Tang, G. Joyce and P. Sprangle, Phys. Fluids B 3, 204 (1991).

33. C. M. Tang, J. Krall and T. Swyden, Phys. Rev. A 45, 7492 (1992).

34. T. P. Hughes and D. Chernin, submitted to Particle Accelerators.

35. D. Chernin and T. P. Hughes, private communication.

36. W. S. Sharp, S. S. Yu and E. P. Lee, private communication.

37. J. Krall, K. Nguyen and G. Joyce, Phys. Fluids B 1, 2099 (1989).

Table I. Parameters for the SLIA POCE: bend design energy E, axial field B_s, quadrupole gradient b_q and quadrupole pitch length λ_p.

Bend	E (MeV)	B_s (G)	b_q (G/cm)	λ_p (cm)
1	4.0	5492.	251.6	68.33
2	5.5	5335.	207.0	83.78
3	7.0	5483.	182.3	125.67

Table II. Numerically determined optimum vertical field values for each POCE bend. Values are in units of Gauss. For comparison, the ideal values (no hoop forces) and the predicted values from Eq. (2) are also given.

Bend	B_v	B_v [ideal]	B_v [δ=1]	B_v [δ=2]
1	233.0	186.9	236.2	248.6
2	296.0	249.5	298.6	311.0
3	354.5	312.5	370.1	372.5

Table III. Location for each bend, each ideal acceleration and each solenoid transition for the end-to-end POCE simulations. Lengths are in centimeters. Note that the acceleration after the third bend is not included and that the POCE design features longer straight sections than those used here.

Bend	Bend location	Acceleration	Solenoid transition
1	50 - 301.3	400 - 450	422.5 - 427.5
2	550 - 801.3	900 - 950	922.5 - 927.5
3	1050 - 1301.3	---	---

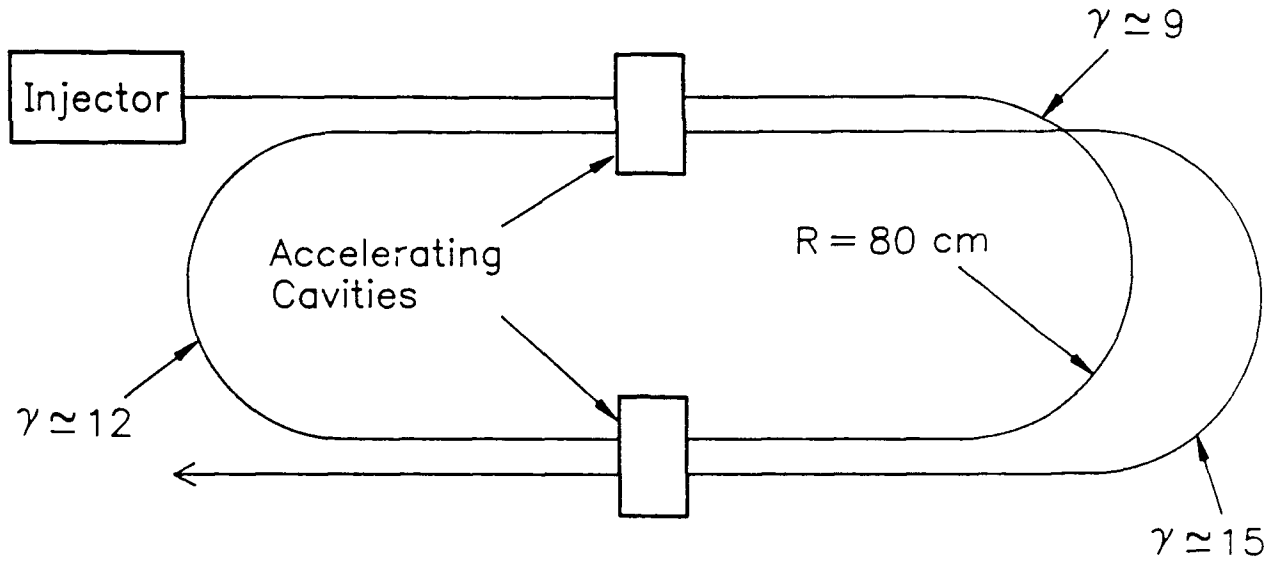

Fig. 1. SLIA proof-of-concept experiment schematic.

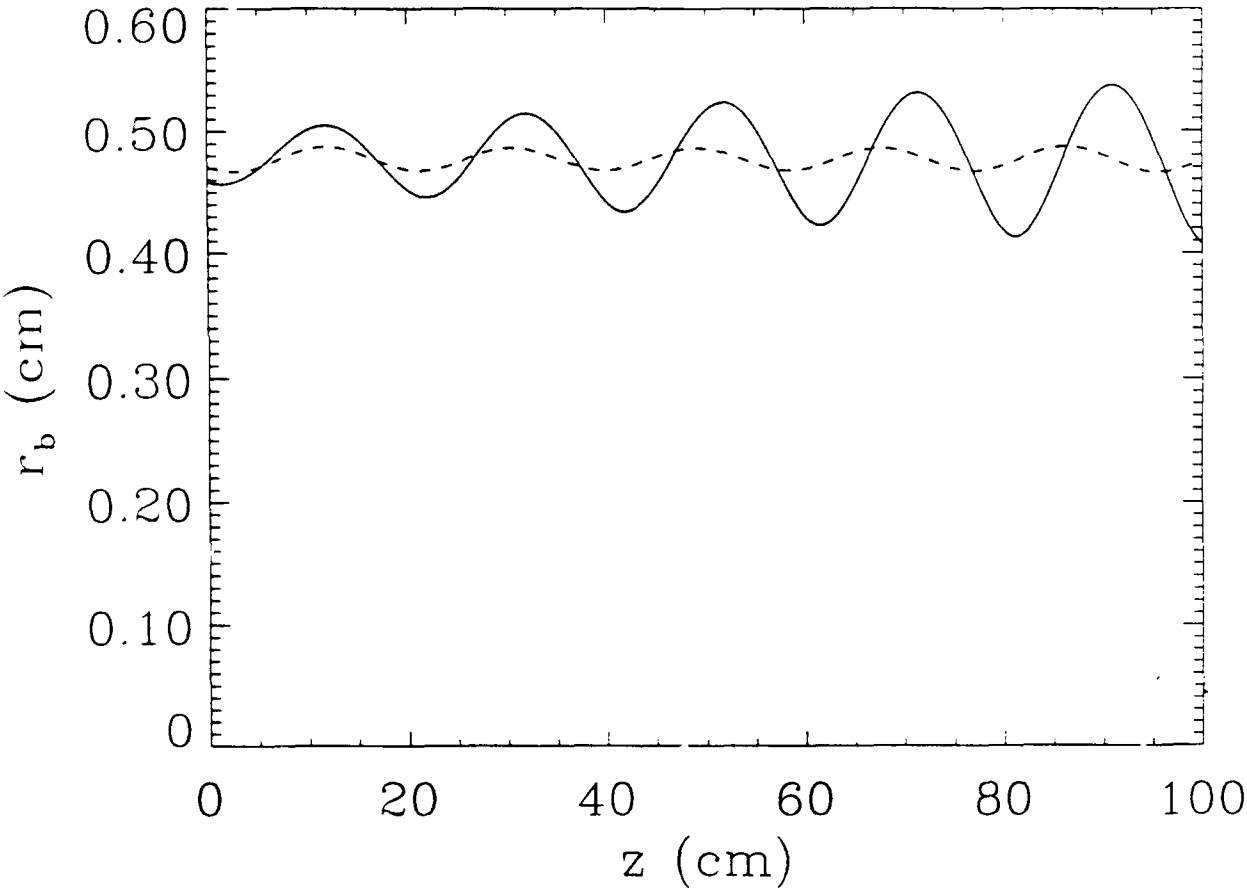

Fig. 2. RMS radius r_b versus transport distance z for the POCE beam initialized with a K-V distribution (solid line) and with a higher-order K-V distribution (dashed line).

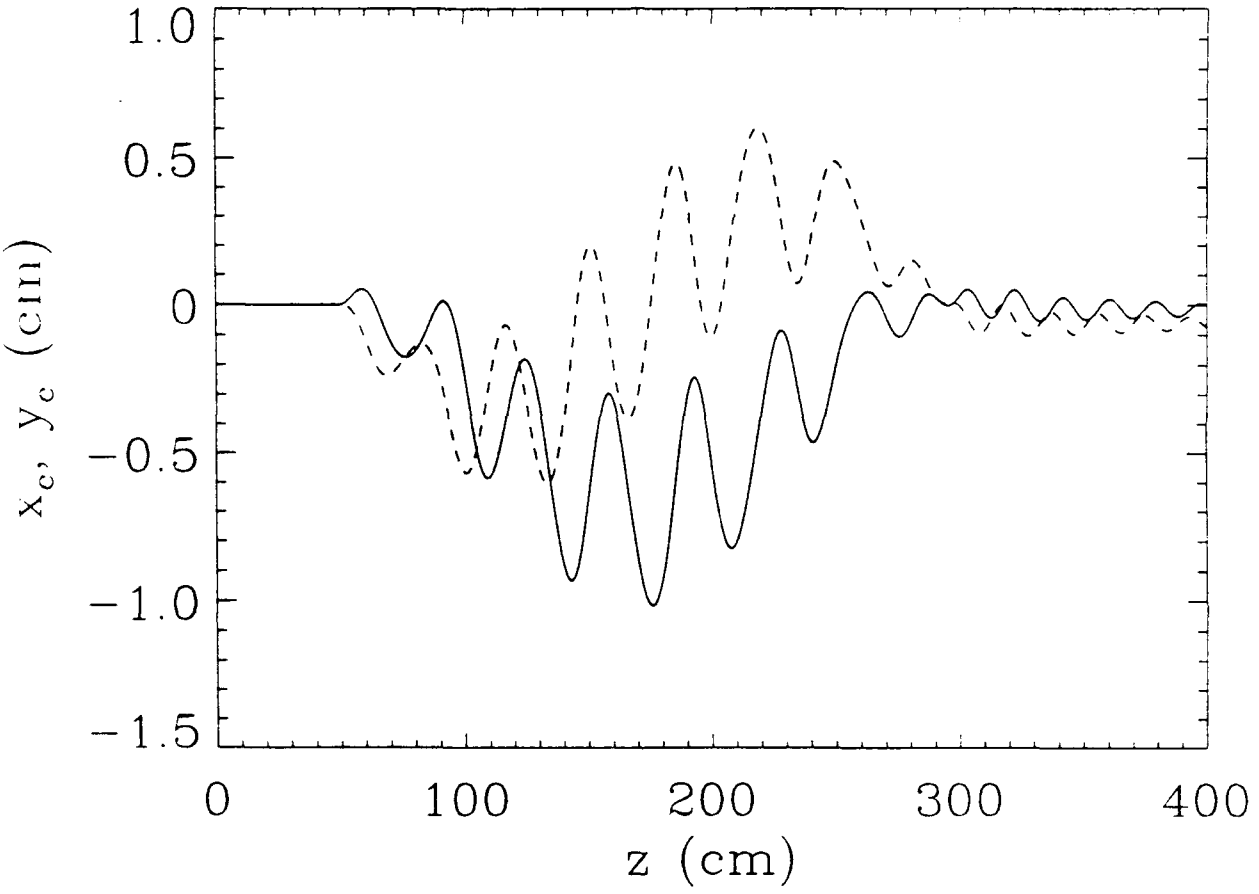

Fig. 3. Beam centroid coordinates x_c (solid) and y_c (dashed) versus transport distance in the first POCE bend with no hoop-force correction. The bend extends from z = 50 cm to z = 301.3 cm.

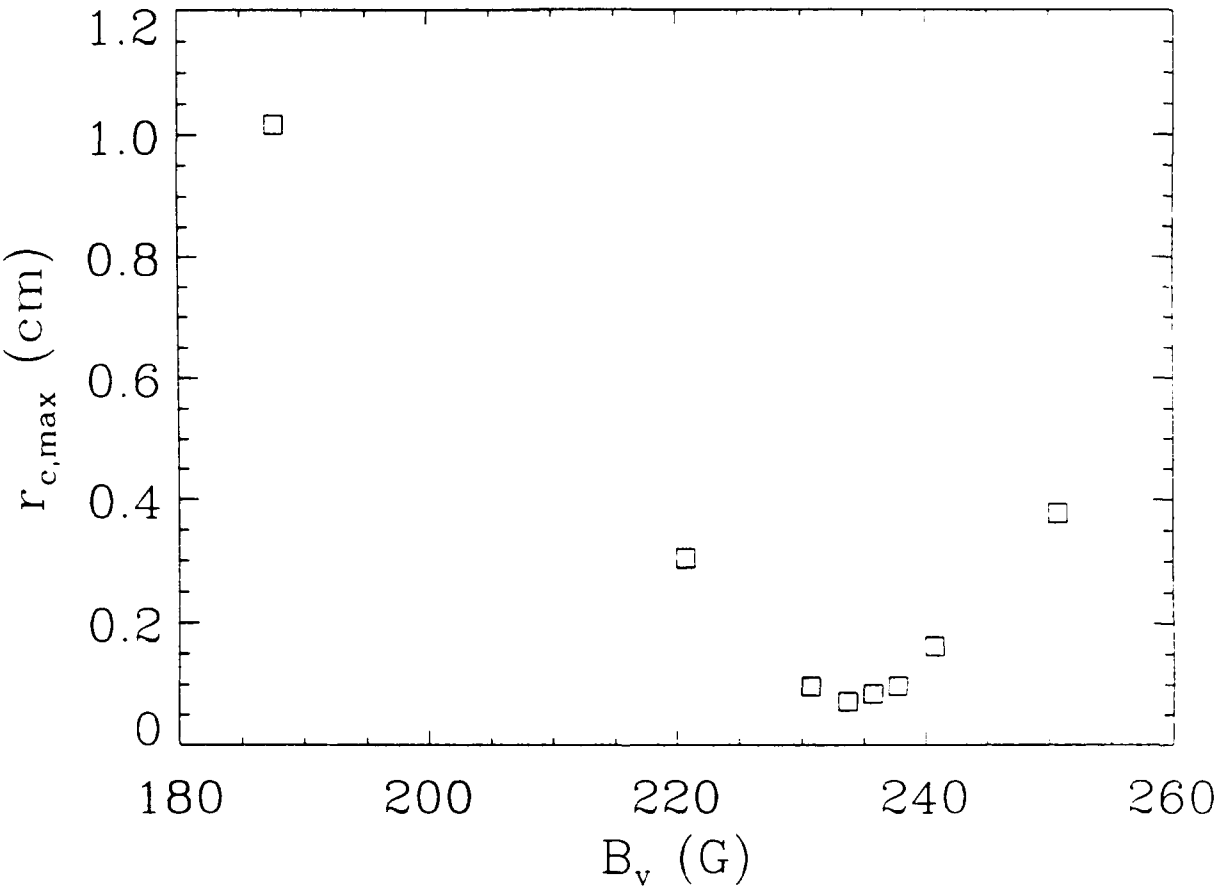

Fig. 4. Maximum displacement of the beam centroid radius, $r_{c,max}$, in the bend versus vertical bending field B_v. Optimum value is B_v = 233 G.

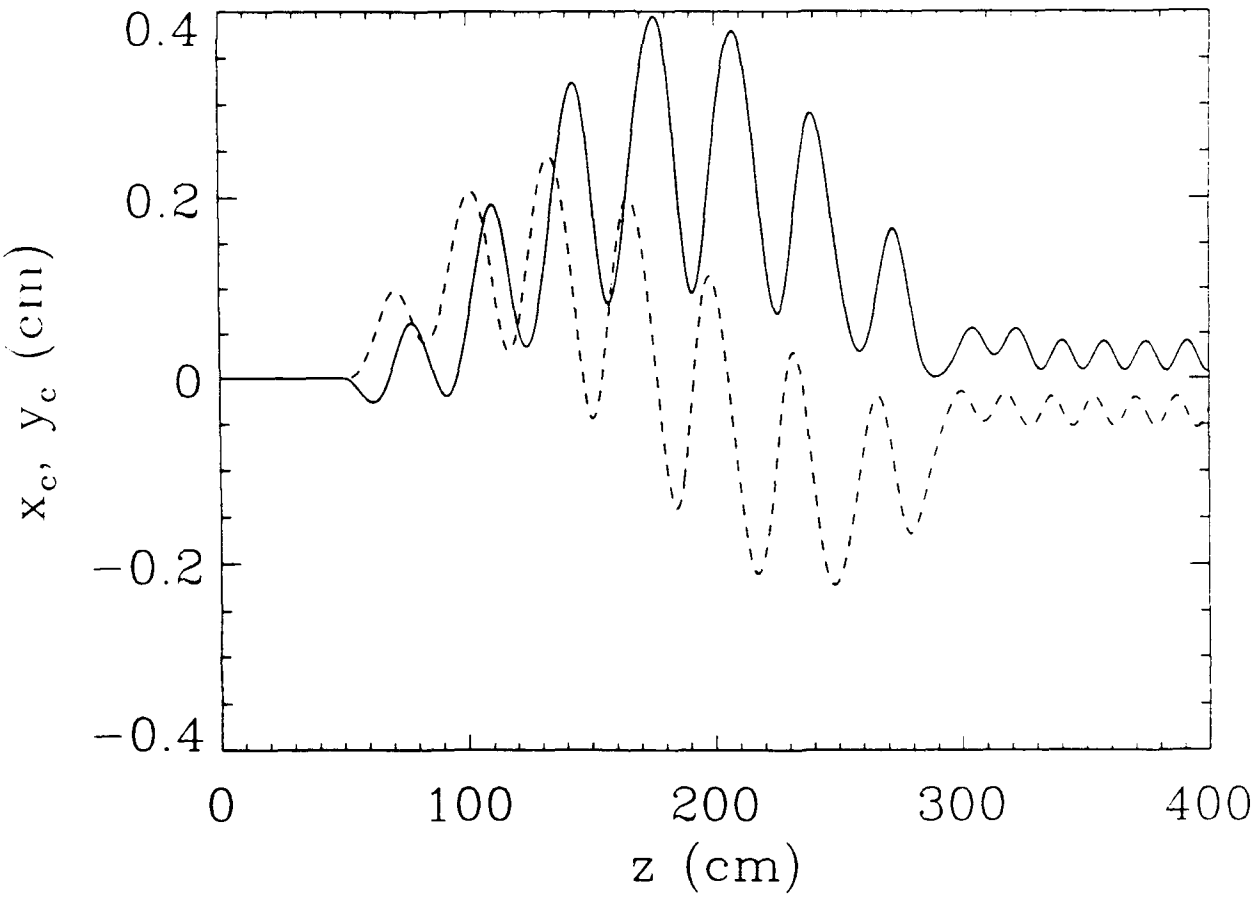

Fig. 5. Beam centroid coordinates x_c (solid) and y_c (dashed) versus transport distance in the first POCE bend with beam energy mismatch $\Delta E = -10\%$.

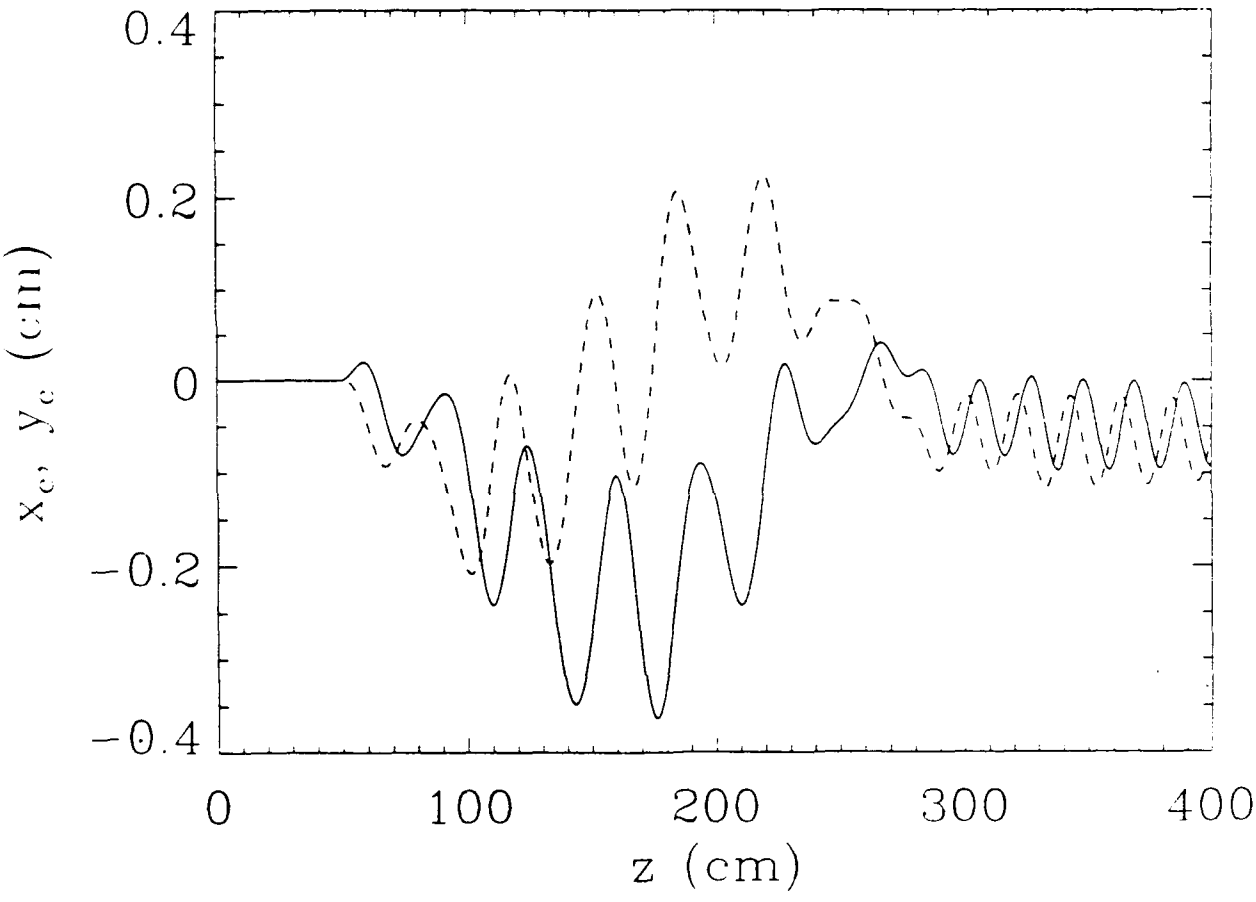

Fig. 6. Beam centroid coordinates x_c (solid) and y_c (dashed) versus transport distance in the first POCE bend with beam energy mismatch ΔE = +10%.

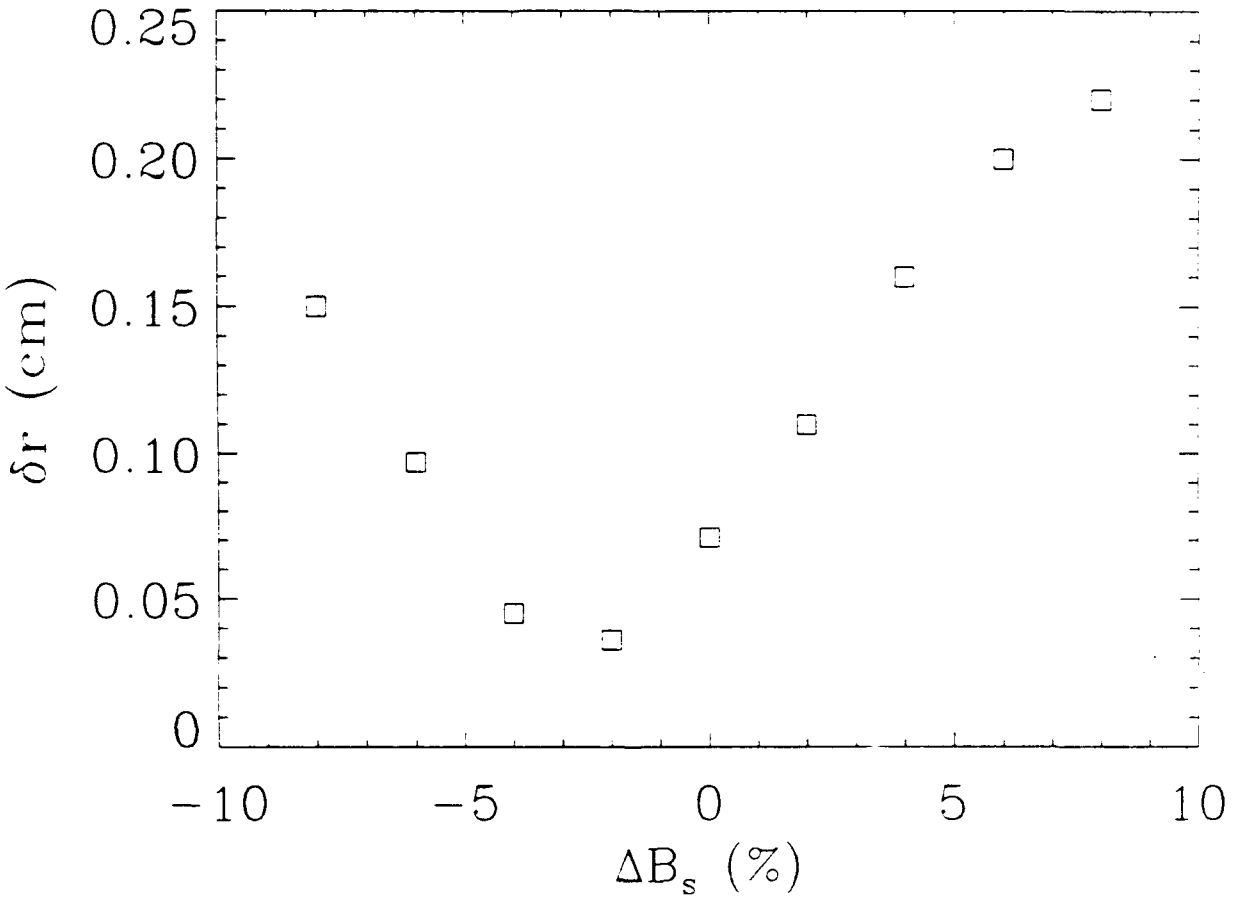

Fig. 7. Beam centroid displacement at the bend exit δr versus percentage error in the axial magnetic field ΔB_s for runs with beam energy mismatch $\Delta E = -10\%$.

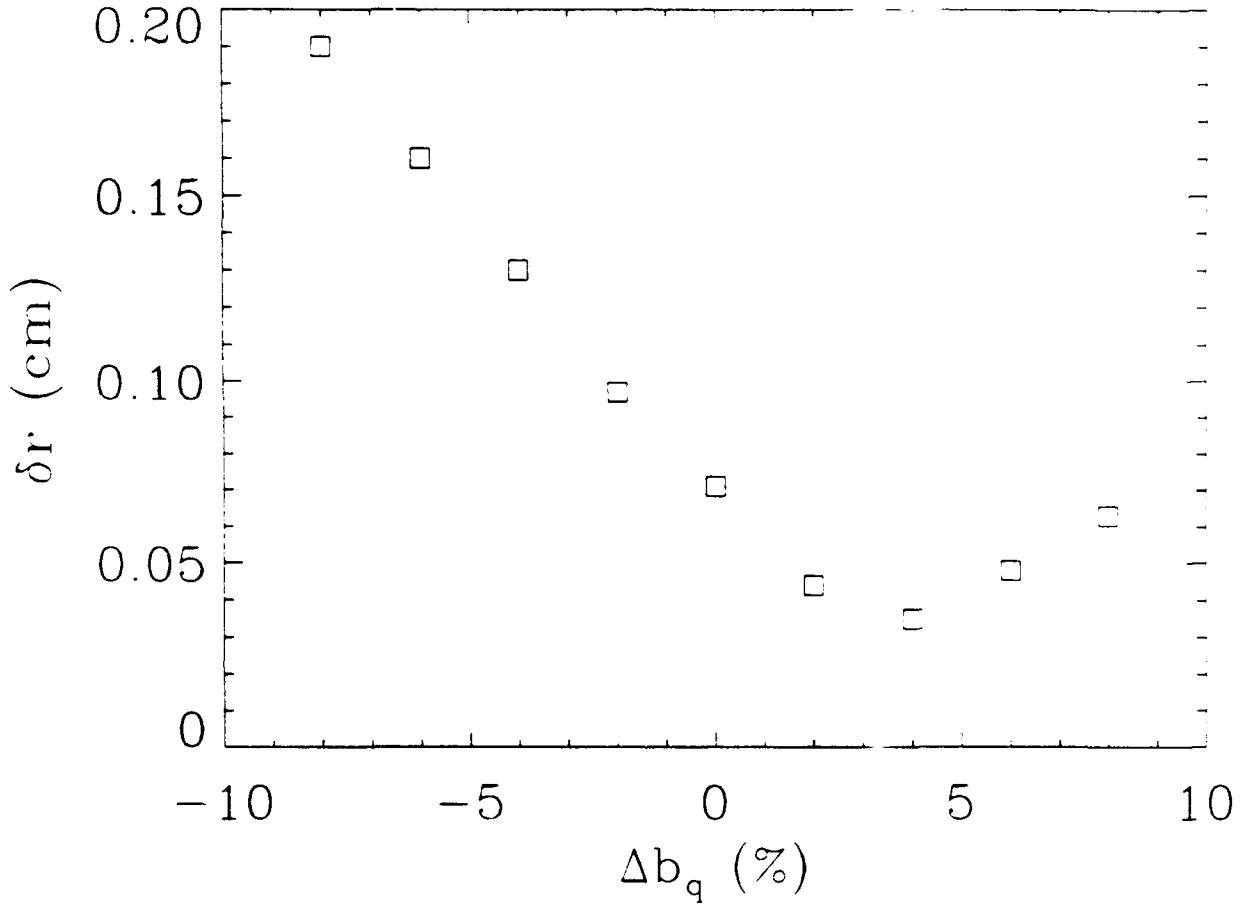

Fig. 8. **Beam centroid displacement at the bend exit δr versus percentage error in the stellarator gradient Δb_q for runs with beam energy mismatch ΔE = -10%.**

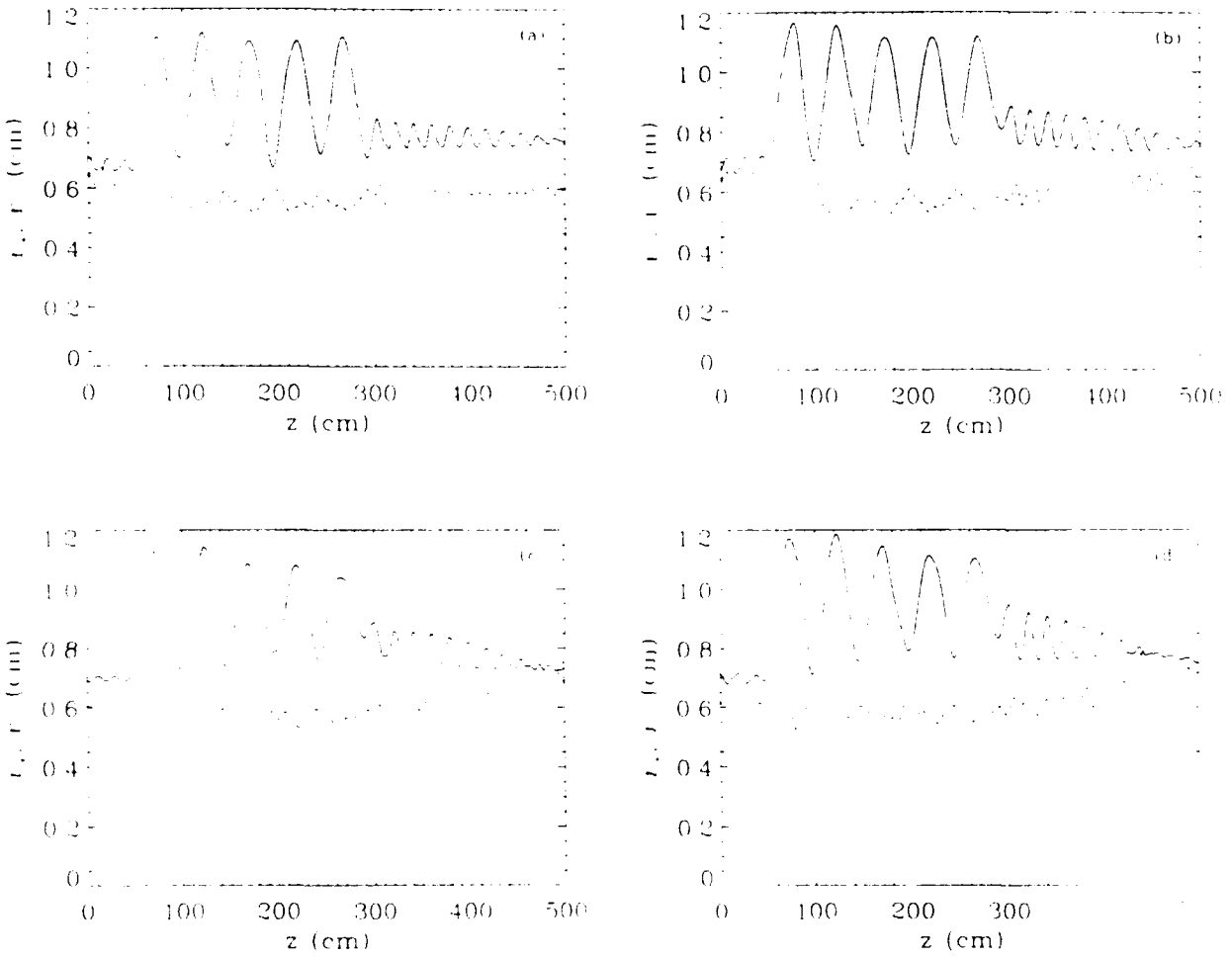

Fig. 9. **Major and minor radii, r_+ (solid) and r_- (dashed), of the beam cross-section versus transport distance for beams with various profiles: (a) K-V, (b) parabolic, (c) Gaussian and (d) Bennett.**

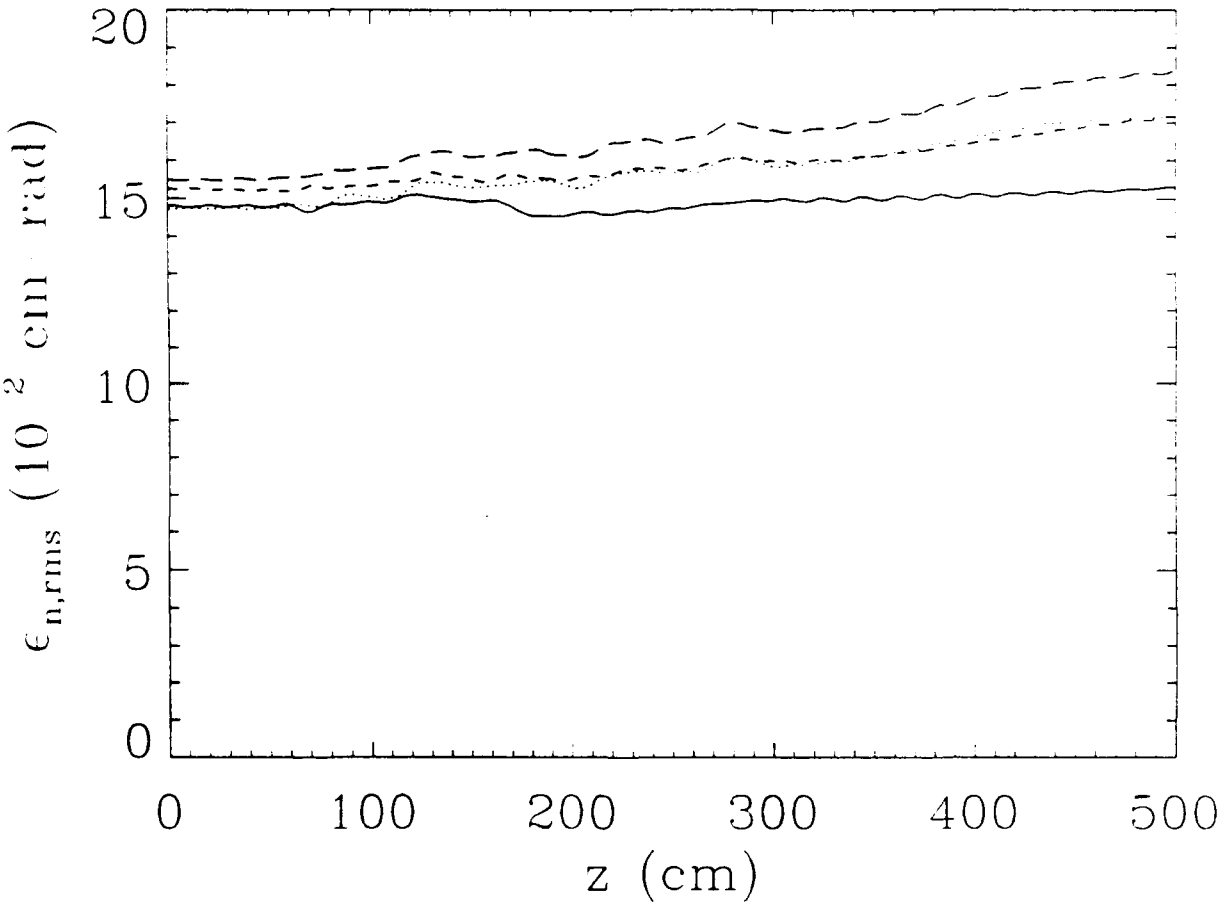

Fig. 10. Emittance $\epsilon_{n,rms}$ versus transport distance for each of the four cases of Fig. 9: K-V (solid line), parabolic (dashed), Gaussian (dotted) and Bennett (long dashes).

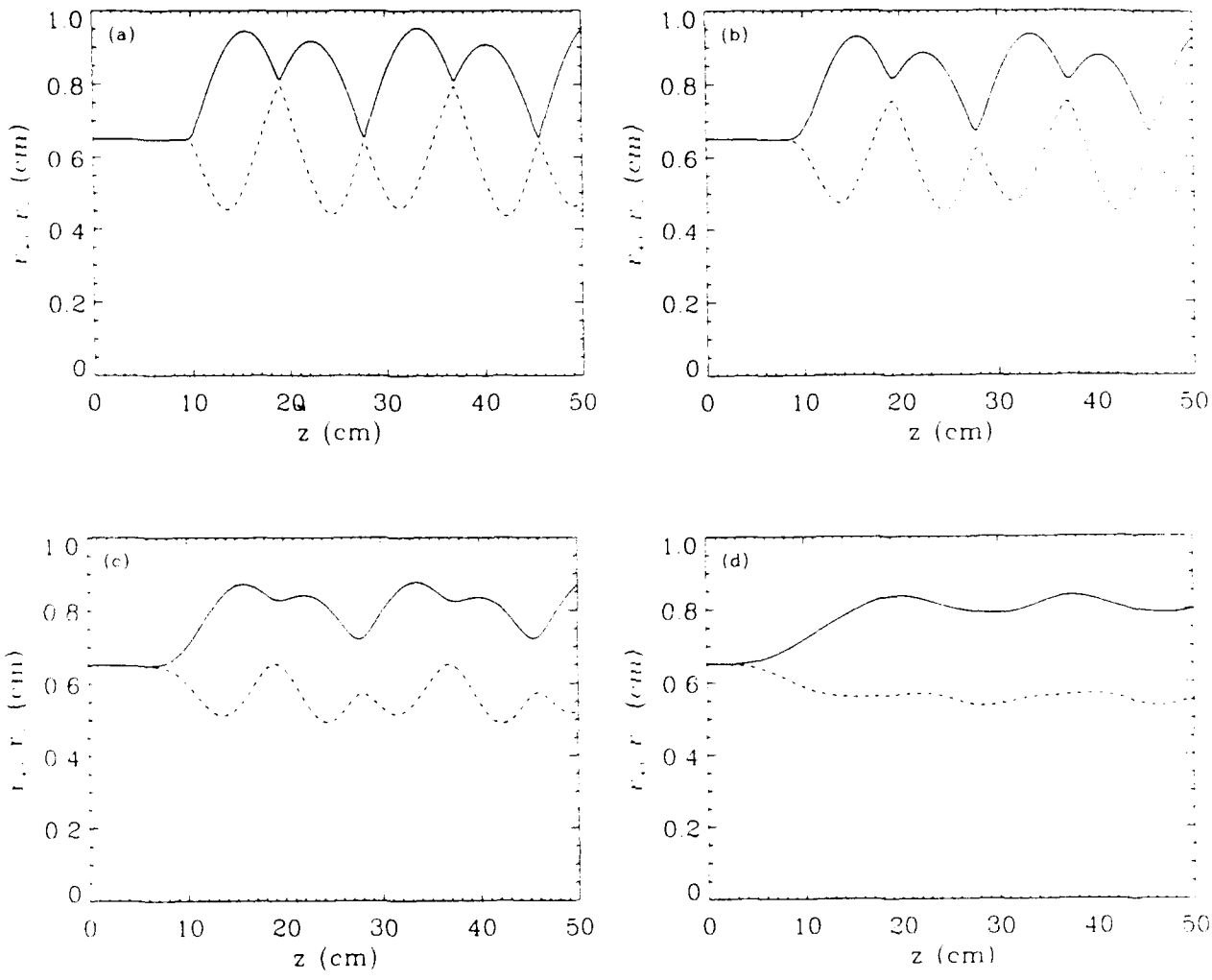

Fig. 11. Envelope code results showing major and minor beam radii versus transport distance for several quadrupole lens lengths L_Q: a) L_Q = 1 cm, b) L_Q = 2.5 cm, c) L_Q = 5 cm and d) L_Q = 10 cm. Here, $L_Q b_Q$ = 2000 G in all cases, where b_Q is the peak quadrupole gradient of the lens. Beam parameters correspond to those of the first POCE bend.

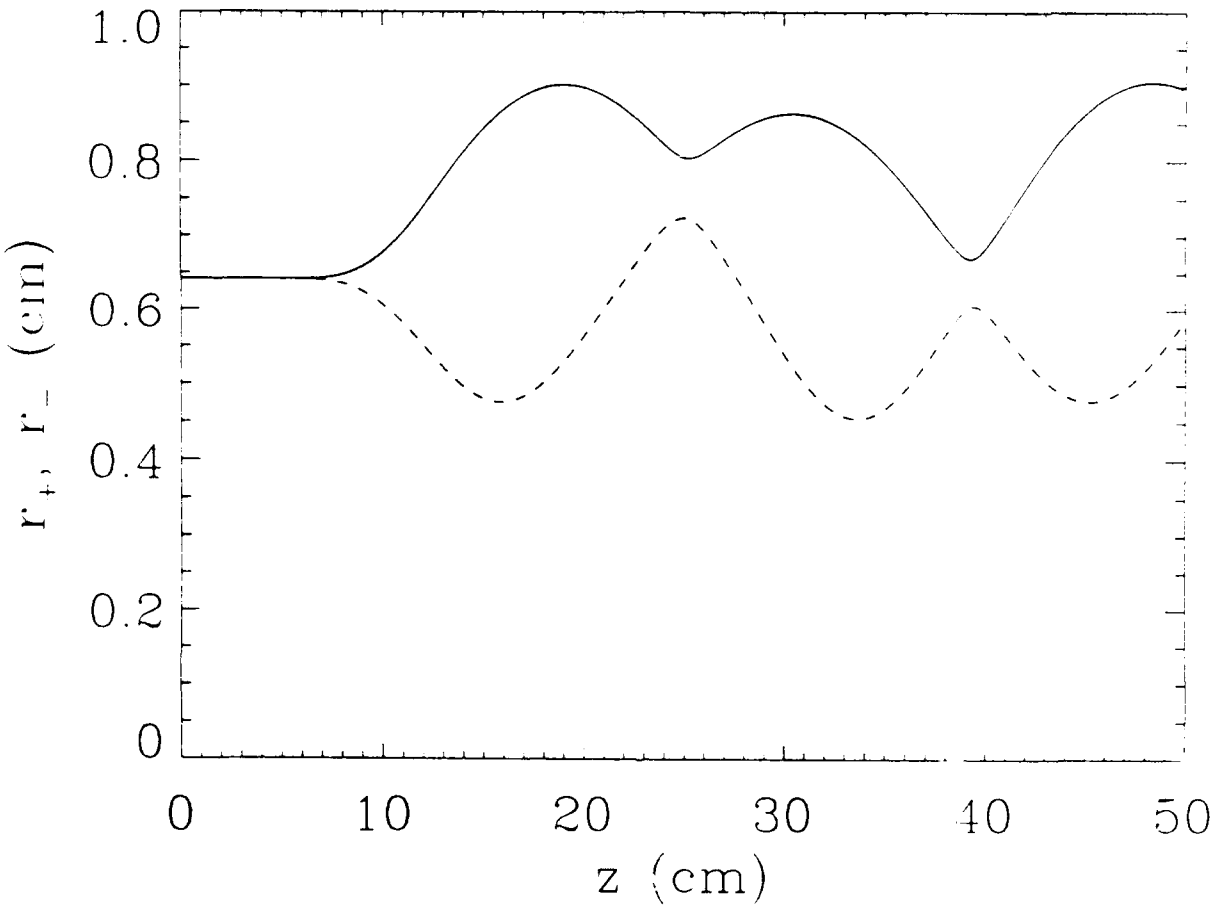

Fig. 12. Envelope code results showing major and minor beam radii versus transport distance for a quadrupole lens with length L_Q = 5 cm and quadrupole gradient b_Q = 400 G/cm as in Fig 11 (c). Beam parameters correspond to those of the third POCE bend.

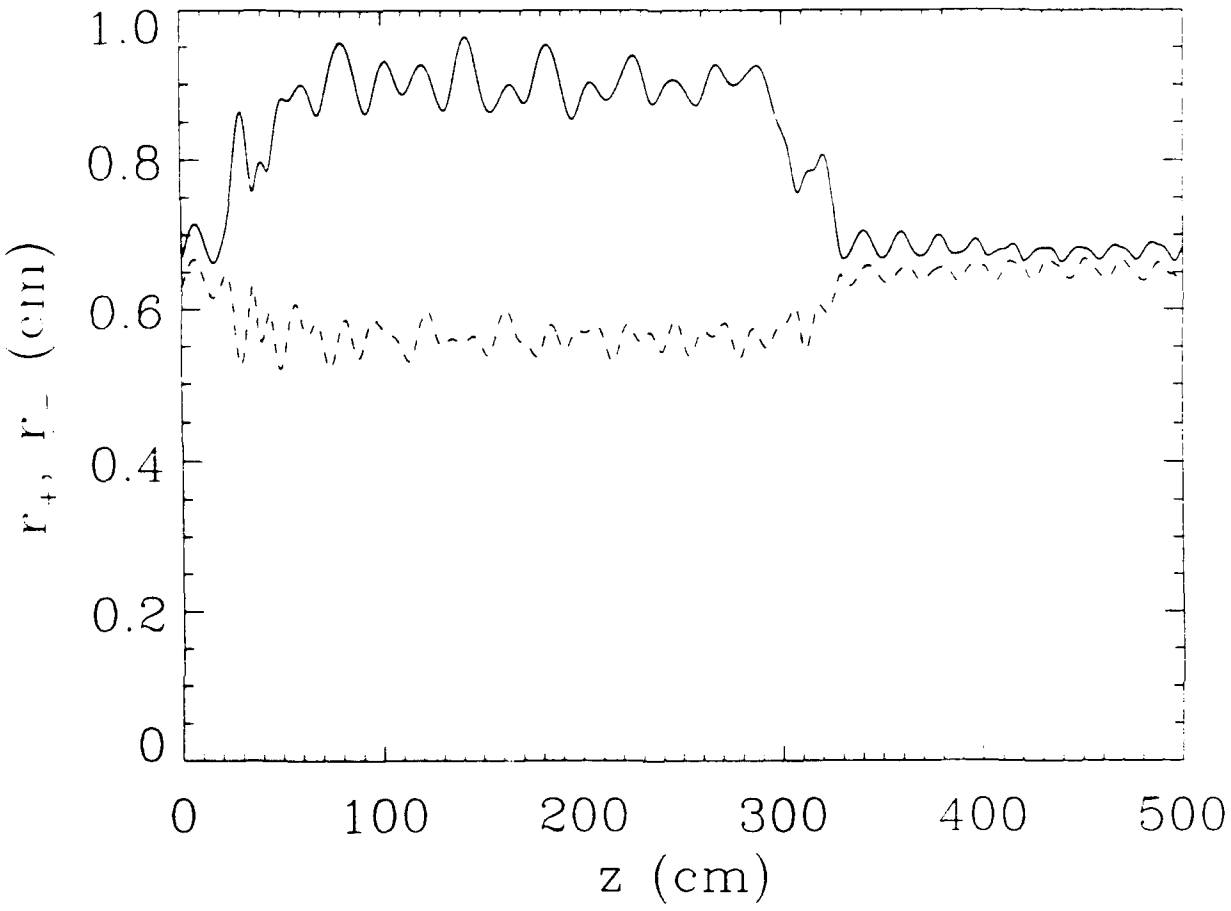

Fig. 13. Simulation result showing major and minor beam radii, r_+ and r_-, as a function of transport distance. Here, single-element matching has been used.

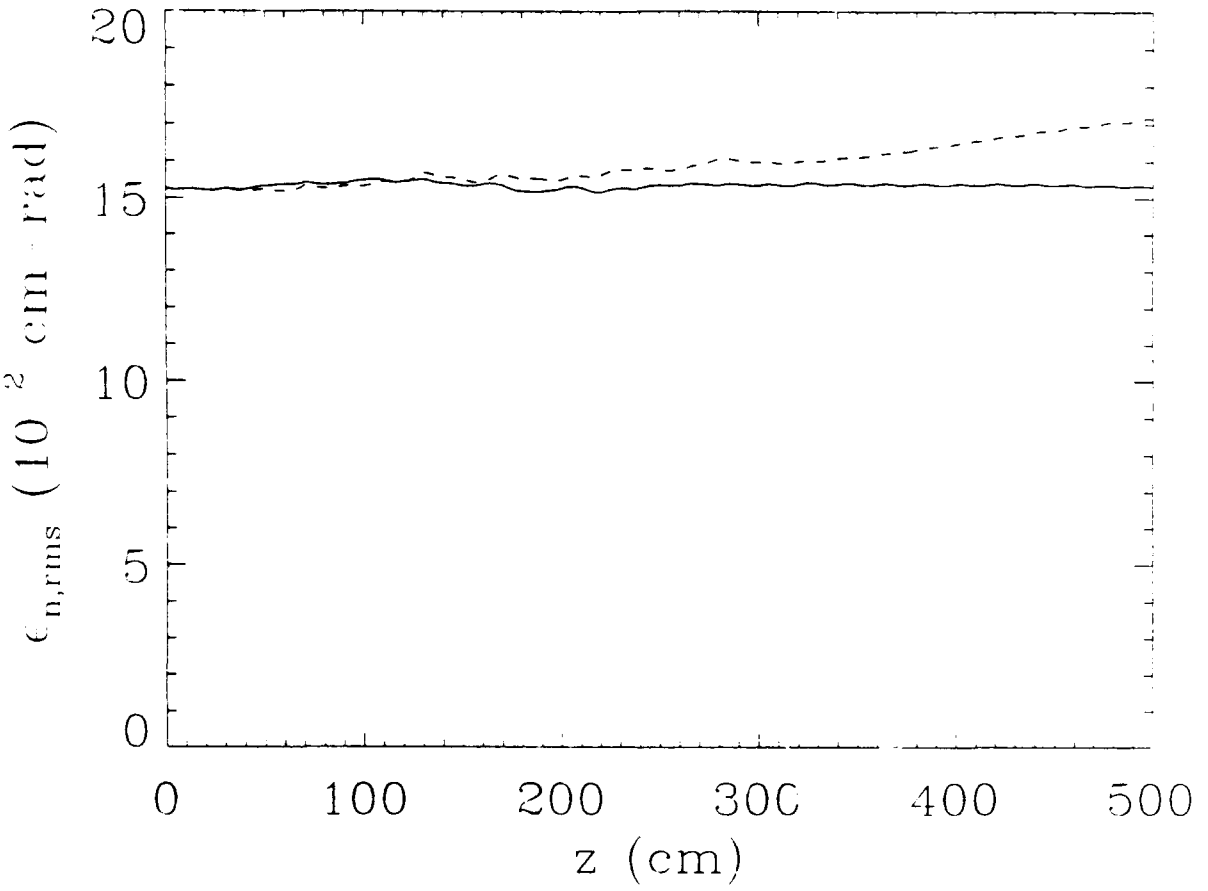

Fig. 14. Simulation result showing normalized RMS emittance as a function of transport distance for the single-element matching case as shown in Fig. 13 (solid line) and for the case with no matching as shown in Fig. 9(b) (dashed line).

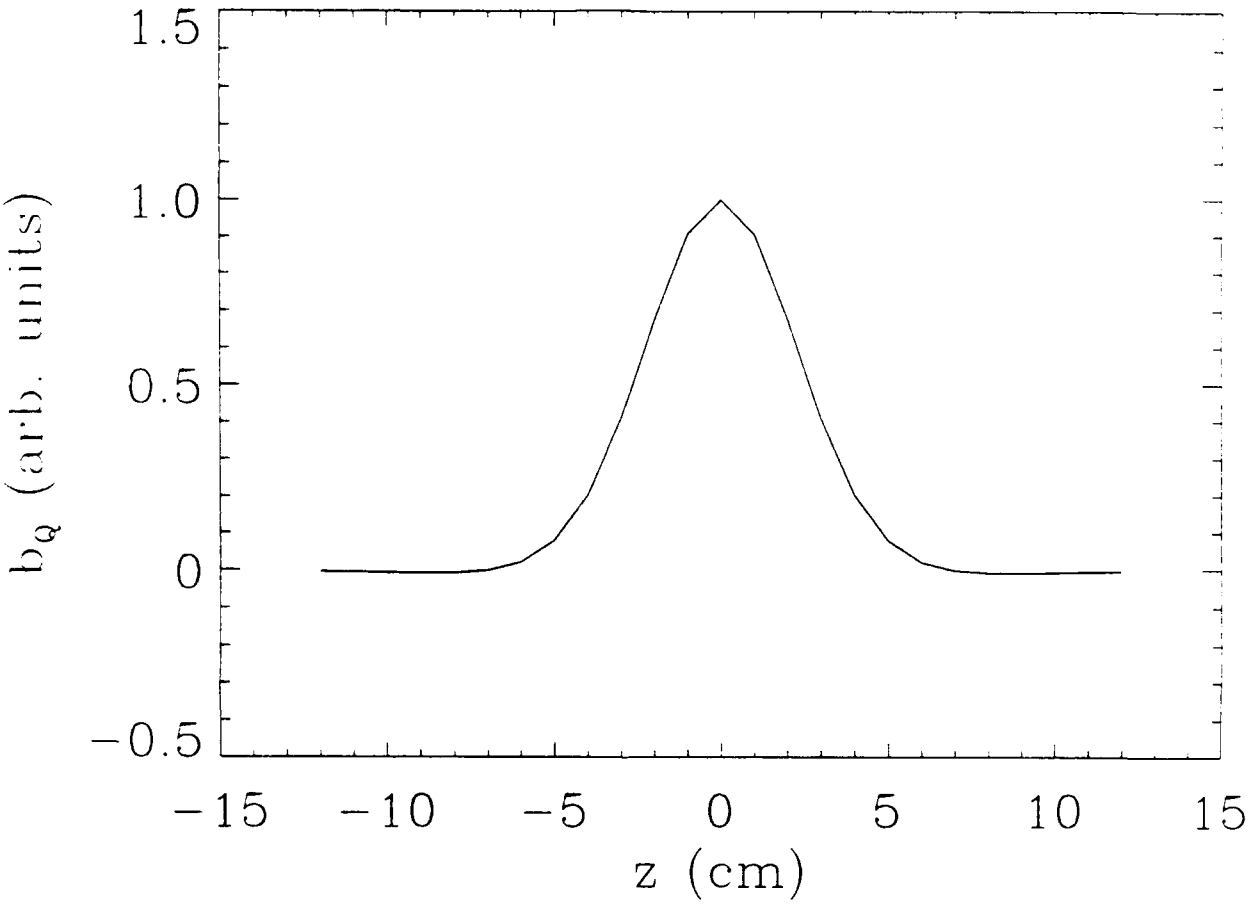

Fig. 15. Quadrupole lens profile versus axial distance.

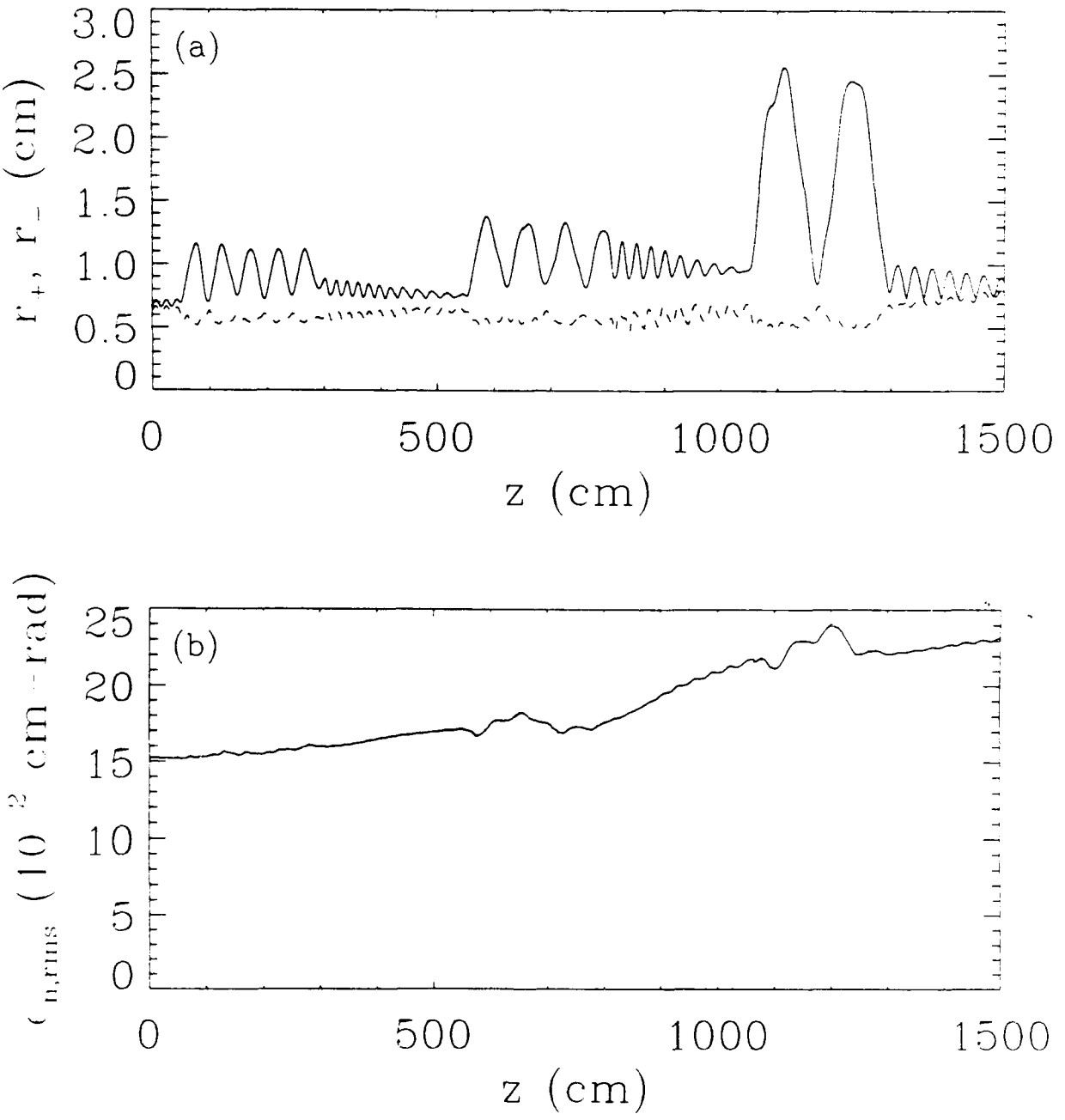

Fig. 16. End-to-end POCE simulation results showing (a) major and minor radii and (b) emittance versus transport distance. No matching lenses are used. The overall emittance growth is 52%.

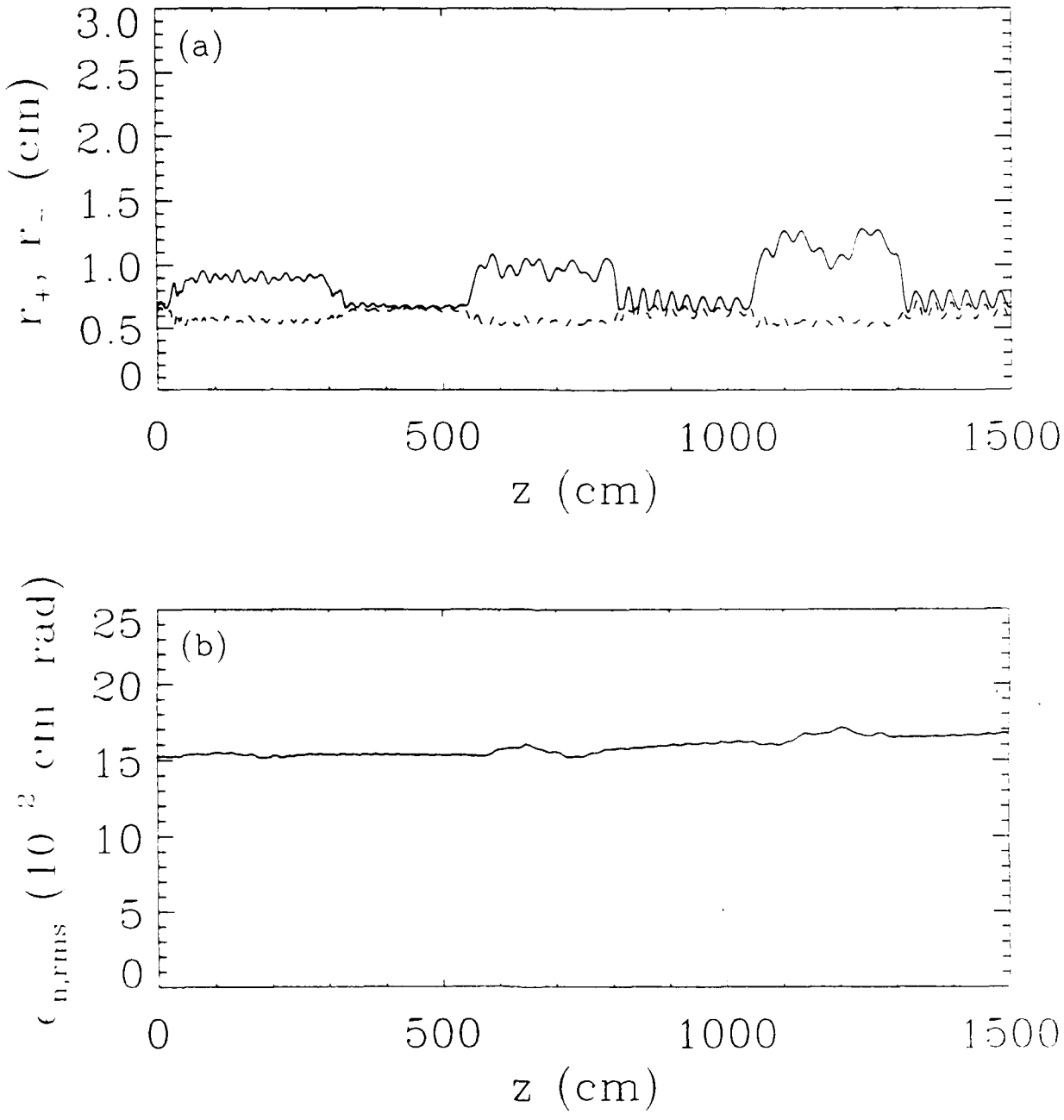

Fig. 17. End-to-end POCE simulation results showing (a) major and minor radii and (b) emittance versus transport distance. Single-element matching lenses are used at the entrance and exit of each bend. The overall emittance growth is 10%.

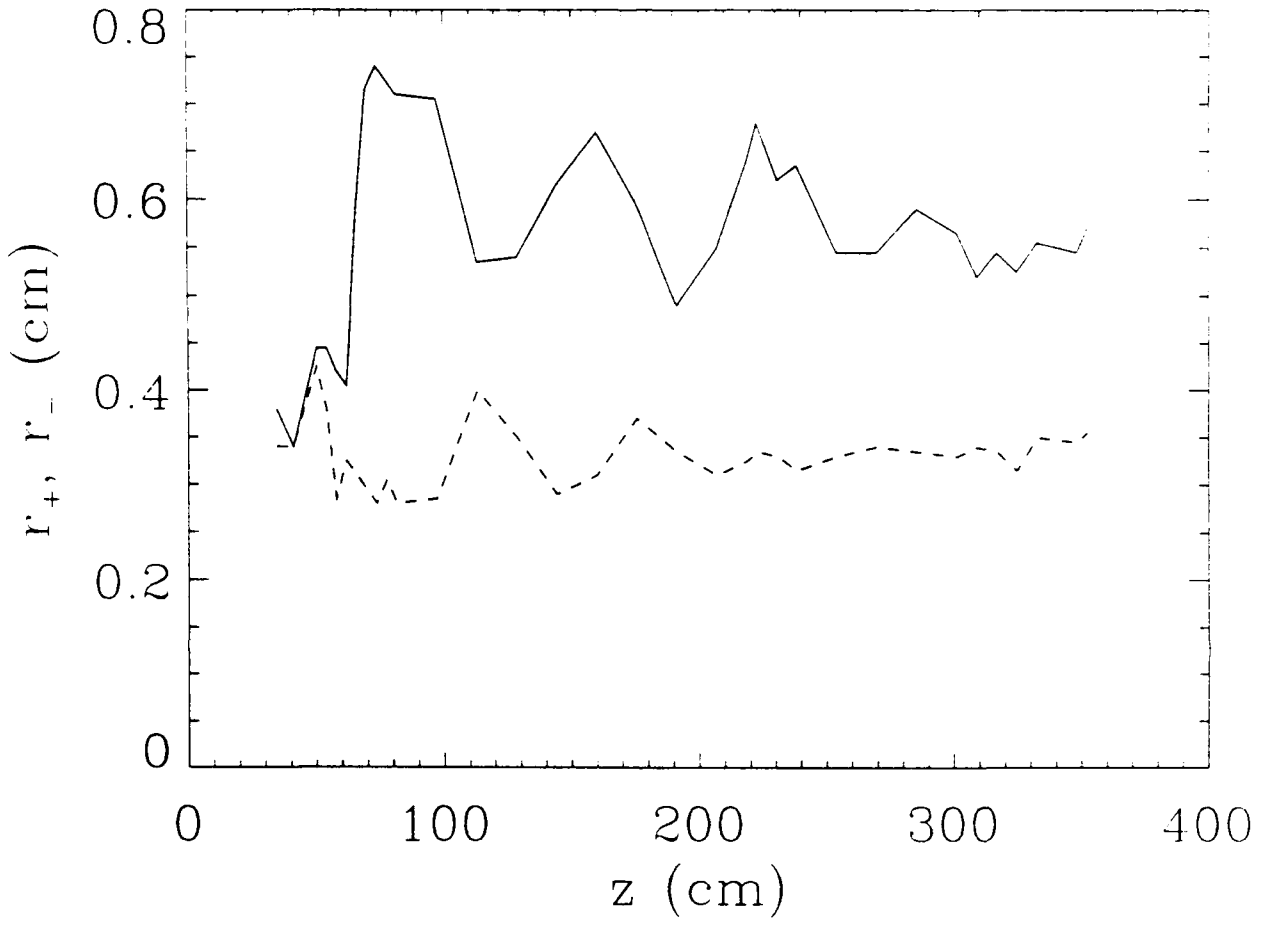

Fig. 18. Experimental data from Lidestri et al.[8] showing the major and minor radii of the beam cross-section as a function of transport distance. In this plot, the stellarator entrance is at z = 50 cm and the exit is at z = 301.3 cm.

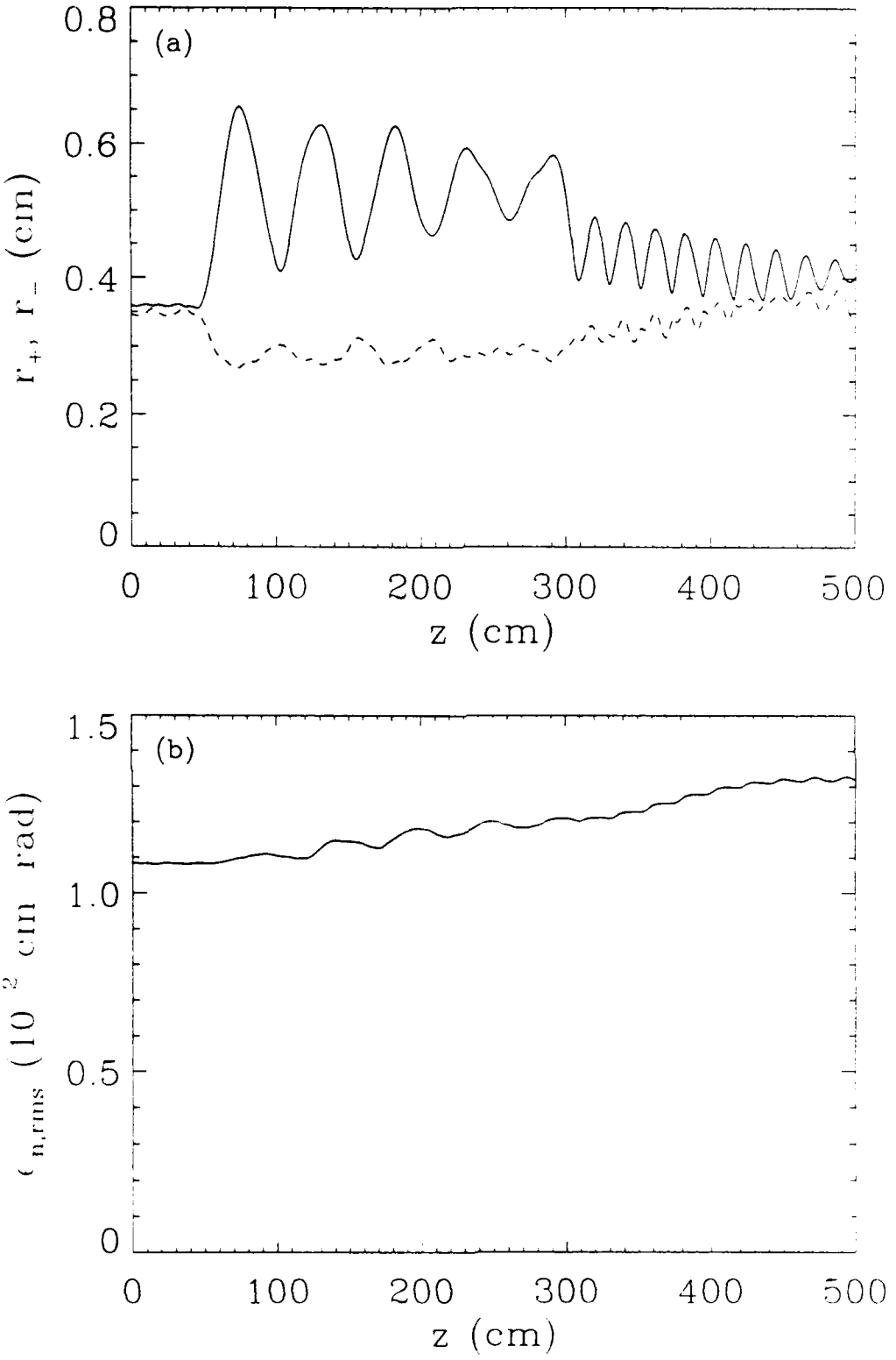

Fig. 19. Simulation result showing (a) major and minor beam radii and (b) normalized RMS emittance as a function of transport distance for a beam with a parabolic spatial profile.

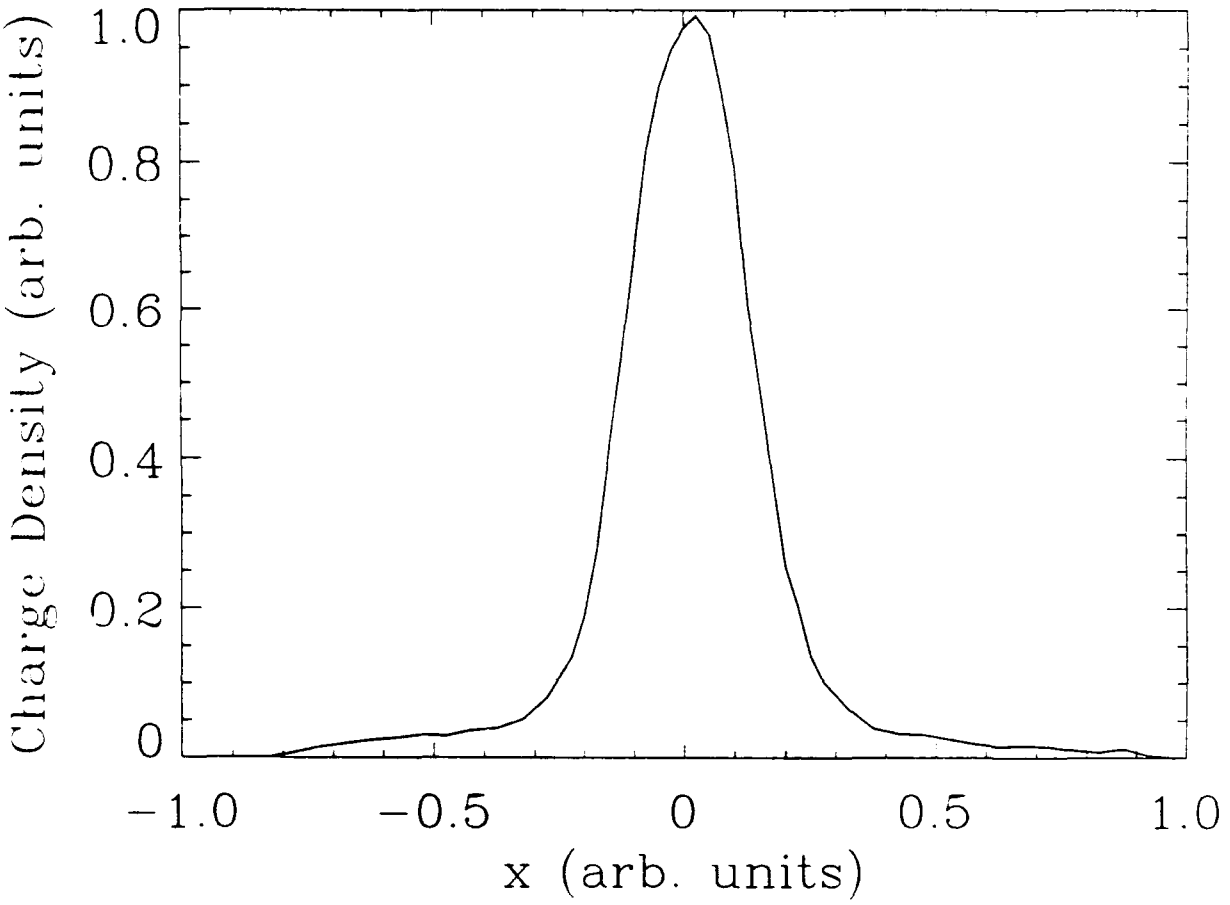

Fig. 20. Experimental data from Tiefenback et al.[10] showing charge density versus transverse coordinate x.

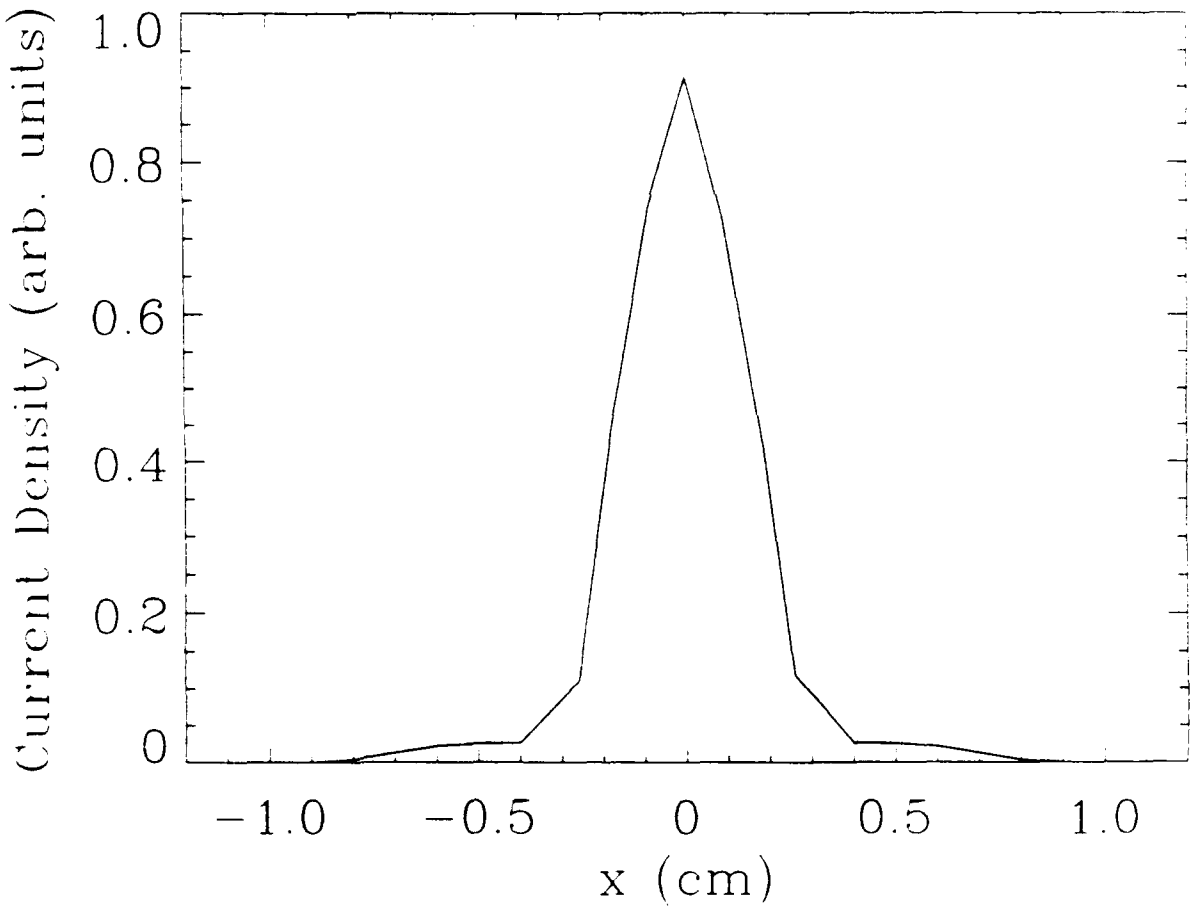

Fig. 21. Current density versus transverse coordinate x for the core-halo simulation beam.

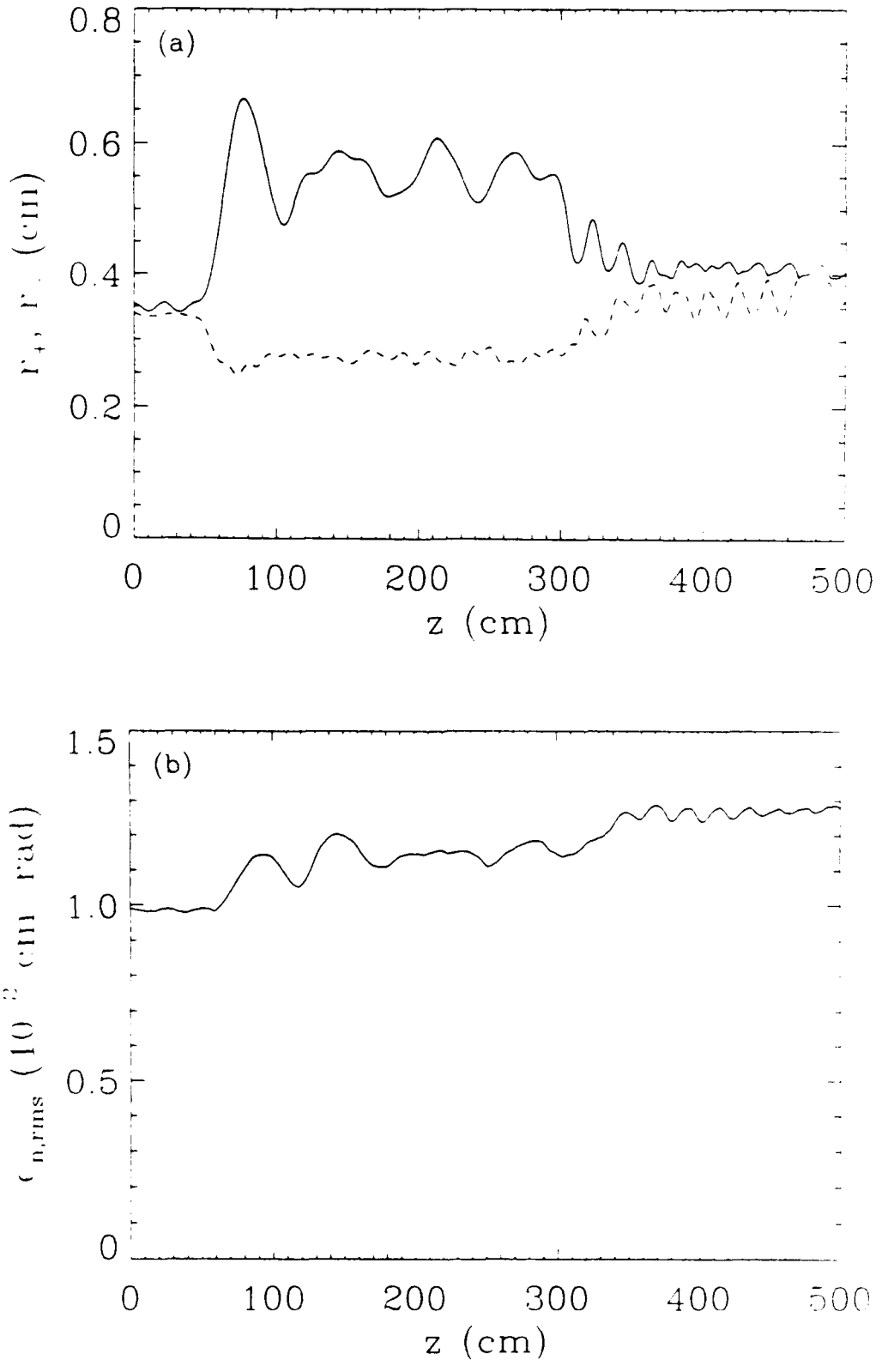

Fig. 22. Simulation result showing (a) major and minor beam radii and (b) normalized RMS emittance as a function of transport distance for a beam with a core-halo distribution.

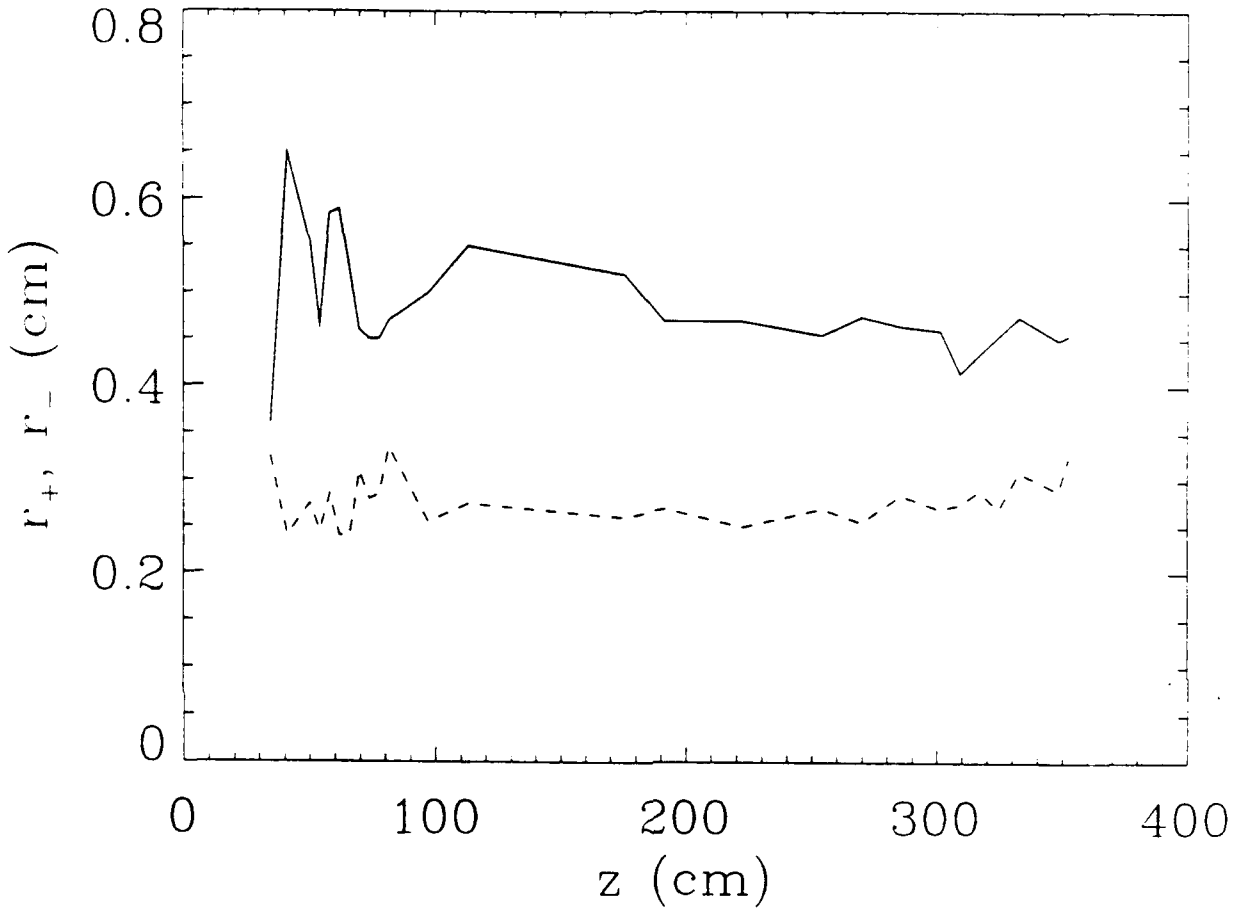
0.8
0.6
0.4
0.2
0
r_+, r_- (cm)
0
100
200
300
400
z (cm)

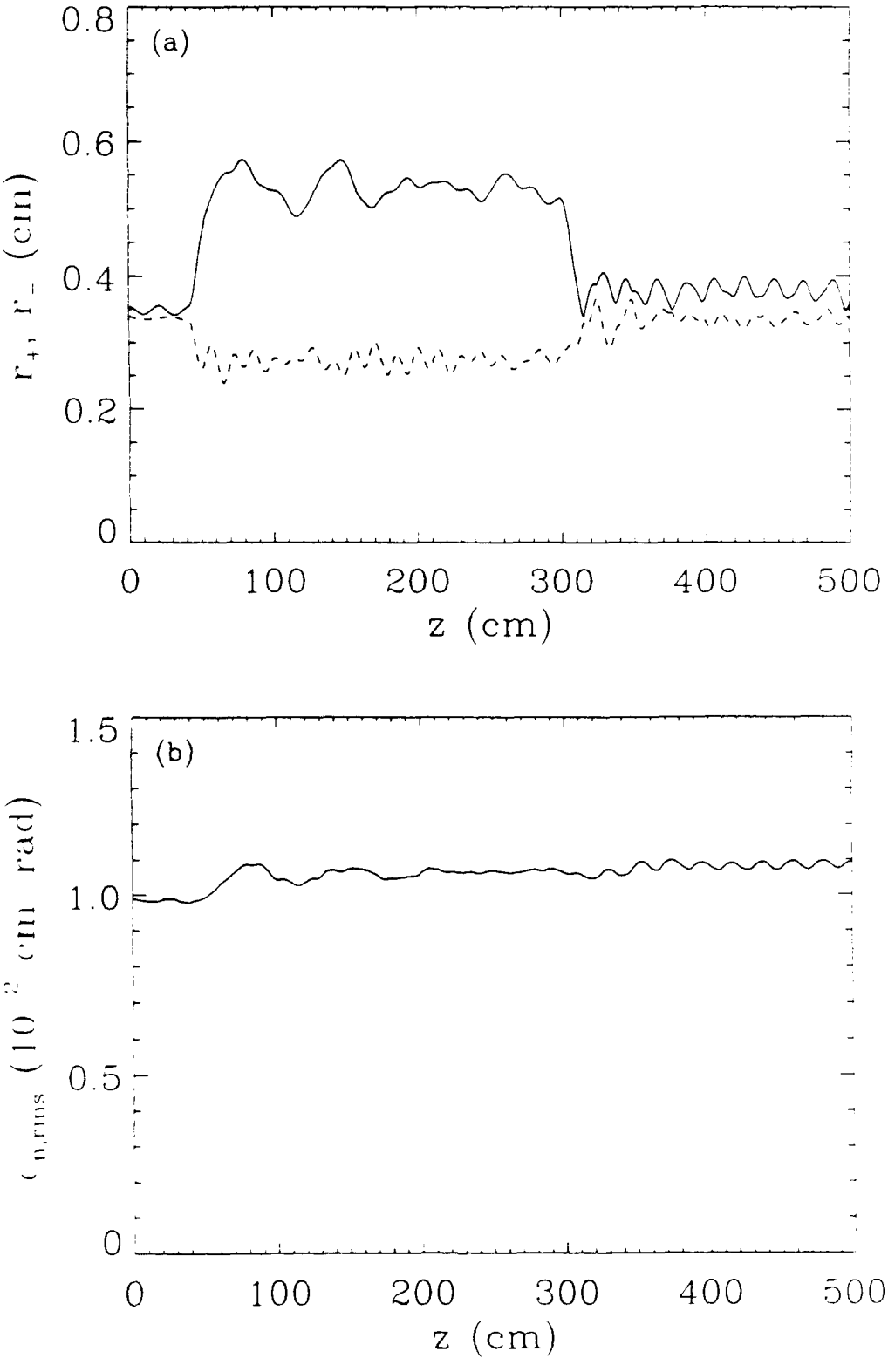

Fig. 24. Simulation result showing (a) major and minor beam radii and (b) normalized RMS emittance as a function of transport distance. In this case, a single-element matching lens was used.